JGR Solid Earth

RESEARCH ARTICLE
10.1029/2025JB031374

Tracing Fluid-Rock Interactions and Migration Pathways in Shallow Megathrust Shear Zones Through Rock Magnetic Analysis

Claudio Robustelli Test[1,2], Dario Bilardello[3], Elena Zanella[1,2], Stefano Ghignone[1], Luca Pellegrino[1], Enzo Ferrara[4], Andrea Festa[1], and Francesca Remitti[5]

[1]Dipartimento di Scienze Della Terra, Università Degli Studi di Torino, Torino, Italy, [2]CIMaN-ALP, Peveragno, Italy, [3]Department of Earth Sciences, Institute for Rock Magnetism, University of Minnesota, Minneapolis, MN, USA, [4]Istituto Nazionale di Ricerca Metrologica, Innovative Materials Metrology and Life Sciences, Torino, Italy, [5]Dipartimento di Scienze Chimiche e Geologiche, Università di Modena e Reggio Emilia, Modena, Italy

Abstract Megathrust shear zones are the main fluid transport pathways during the seismic cycle and play a key role in controlling physicochemical alteration. Defining fluid-rock interaction in wall rocks provides evidence for unraveling the hydrogeology of shear zones and their link to active fluid circulation. We analyzed the variation in concentration, grain size and assemblages of magnetic minerals in the wall rocks of a shallow megathrust (the Sestola Vidiciatico shear zone) where no evidence of high-frictional heating has been recorded. The Sestola Vidiciatico shear zone preserves evidence of active fluid circulation and stress-switch during the last brittle phases of the Early to Middle Miocene subduction of the Adriatic plate beneath the frontal prism of the European plate. Magnetic properties indicate low bulk heat transfer during the seismic cycle. Changes in magnetic mineral concentrations highlight iron depletion from clay minerals and dissolution of iron-oxides for interaction with exotic fluids during the coseismic phase. The relative distribution of Fe-oxides and goethite suggests migration of Fe-enriched fluids along fractures during the coseismic/postseismic phase, followed by precipitation for interaction with local fluids. Subsequent alteration and weathering of magnetic minerals, accompanied by the formation of hematite and maghemite, are related to partial oxidation during the interseismic phase. Heterogeneity in magnetic mineral distribution supports active fluid circulation during repeated seismic events and/or exhumation. Rock magnetic characterization of wall rocks in exhumed megathrust represents a promising tool to better understand the role of fluid migration and redox conditions during seismic cycles in subduction zones.

Plain Language Summary Megathrust shear zones are key pathways for fluid movement during earthquakes. When fluids interact with the surrounding rocks, they cause changes in the physical and chemical properties of the rocks. Studying the magnetic properties of rocks along these zones can provide valuable insights into fluid movement and chemical changes during earthquakes. In our study, changes in magnetic properties suggest the circulation of fluids in disequilibrium through fractured zones during earthquakes, causing iron loss from clay minerals and dissolution of magnetic minerals. After earthquakes, interactions with local fluids lead to precipitation of new minerals and the alteration of existing magnetic minerals.

Key Points:

- Variations in concentration, grain size and assemblages of magnetic minerals reveal fluid migration pathways along a shallow megathrust
- Coseismic exotic fluids in disequilibrium with the wall rocks are responsible for depletion of clay minerals and dissolution of Fe-oxides
- Lithological variations control the preservation of diagenetic features and alteration/oxidation products during interseismic periods

Supporting Information:

Supporting Information may be found in the online version of this article.

Correspondence to:

C. Robustelli Test,
claudio.robustellitest@unito.it

Citation:

Robustelli Test, C., Bilardello, D., Zanella, E., Ghignone, S., Pellegrino, L., Ferrara, E., et al. (2025). Tracing fluid-rock interactions and migration pathways in shallow megathrust shear zones through rock magnetic analysis. *Journal of Geophysical Research: Solid Earth*, *130*, e2025JB031374. https://doi.org/10.1029/2025JB031374

Received 12 FEB 2025
Accepted 9 SEP 2025

Author Contributions:

Conceptualization: Claudio Robustelli Test
Writing – original draft: Claudio Robustelli Test, Dario Bilardello, Elena Zanella
Writing – review & editing: Dario Bilardello, Elena Zanella, Stefano Ghignone, Luca Pellegrino, Enzo Ferrara, Andrea Festa, Francesca Remitti

1. Introduction

In active convergent margins, intraplate shear zones at shallow levels, including megathrusts, represent preferential migration pathways for large volumes of fluid (e.g., Moore & Vrolijk, 1992; Ranero et al., 2008; Saffer & Tobin, 2011). Fluids transport heat and elements, interact with the wall rock, and lead to mineral transformations and precipitation, which in turn induce changes in the physicochemical and mechanical properties of fault rocks (Fulton & Brodsky, 2016; Meneghini et al., 2020; Sibson, 2013; Vannucchi et al., 2012). In exhumed intraplate shear zones and megathrusts, several studies have analyzed the internal texture (Meneghini et al., 2007; Mittempergher et al., 2018; Vannucchi et al., 2008, 2009), fluid inclusions (Moore et al., 2007; Raimbourg et al., 2018) and geochemistry of tectonic veins, revealing active fluid circulation related to major seismic cycles, with cyclical variations in permeability, pressure regimes, fluid sources, and redox conditions (e.g., Cerchiari et al., 2020; Ujiie & Kimura, 2014; Vannucchi et al., 2010; Yamaguchi et al., 2011). Geochemical and isotopic records in calcite veins testify both the localized transport of external exotic fluids along faults and evidence of postseismic local buffering (i.e., Cerchiari et al., 2020). Integration with wall rock geochemistry and

microstructure analyses provides a continuous record of fluid-rock interaction pathways during the seismic cycle (Charpentier et al., 2024; Raimbourg et al., 2018; Tartaglia et al., 2020). In addition, changes in relative concentrations, grain size, and assemblages of magnetic minerals, as revealed by rock magnetic measurements, can provide high-resolution insights into changes in the physicochemical conditions (e.g., redox conditions, pH of fluids, and temperature) that occurred in the wall rocks during coseismic, postseismic and interseismic phases (e.g., Chen et al., 2019; Chou et al., 2012; Greve et al., 2021; Yang, Yang, et al., 2016), as well as upon weathering (Liu et al., 2022).

The interaction between fault rock and circulating fluids can induce selective dissolution of Fe-bearing minerals, enriching the fluids in Fe^{2+} and resulting in the precipitation of new minerals such as fine-grained iron-oxides (e.g., magnetite), iron-oxyhydroxides (e.g., goethite), and/or sulfides (e.g., pyrite or pyrrhotite), leading to changes in magnetic properties (e.g., Yang et al., 2020). Increased susceptibility and magnetization of fault rocks has been widely linked to the enrichment of newly formed ferrimagnetic minerals (Chou et al., 2012; Mishima et al., 2009; Tanikawa et al., 2008; Yang, Yang, et al., 2016). In contrast, decreased susceptibility and magnetization proxies have been observed in proximity of fault-zones, suggesting magnetite depletion and Fe^{2+} incorporation in Fe-rich clay minerals (Yang, Dekkers, & Zhang, 2016). Low concentrations of ferrimagnetic minerals may also result from anaerobic oxidation of methane during drainage of fluids, reducing greigite to paramagnetic pyrite (Greve et al., 2021), under these conditions, fine-grained (SD) magnetite is dissolved as well. Percolation of hot acqueous fluids ($T > 350$°C) during coseismic phases leads to alteration/transformation of pyrite to pyrrhotite, siderite to magnetite, and to partial oxidation of magnetite (Chou et al., 2012; Tanikawa et al., 2008; Yang et al., 2018). Additionally, cooling of hot coseismic fluids has been observed to induce goethite enrichment (Chou et al., 2012). Finally, localized and intense shearing can result in mechanical grain size reduction of ferromagnetic s.l. particles from multidomain (MD) to single domain (SD) or even superparamagnetic (SP), with magnetic properties changing as grain size and grain internal stress vary (e.g., Jackson et al., 1993; Till et al., 2012). In particular, grain size reduction of ferrimagnetic particles to SP state can lead to increased susceptibility (Chou et al., 2014; Hirono et al., 2006; Yang et al., 2020).

So far, most rock magnetic studies have focused on shear zones that experienced seismic frictional heating to estimate the peak temperature along slip surfaces (e.g., Hirono et al., 2009; Mishima et al., 2006; Yang, Dekkers, & Zhang, 2016) and to investigate thermal decomposition of Fe-bearing minerals linked to increased susceptibility (e.g., Chou et al., 2012; Mishima et al., 2009; Tanikawa et al., 2008; Yan et al., 2023). This study investigates how fluid circulation may have induced variations in magnetic properties in two sectors of an exhumed megathrust shear zone that experienced low maximum temperatures (120–150°C) and where no evidence of frictional heating or high-temperature alteration was identified (Remitti et al., 2013; Vannucchi et al., 2008). We discuss variations in magnetic mineral assemblages of wall rocks and changes in their concentration and grain size at increasing distances from localized fluid transport and vein precipitation zones. Additionally, we explore the potential for rock magnetic techniques to record fluid-rock interaction processes (e.g., alteration, leaching, and neoformation of minerals), and to trace fluid pathways during seismic cycles.

2. Geological Setting and Background

The Sestola-Vidiciatico tectonic Unit (SVU), exposed in the Northern Apennines (Italy; Figure 1), represents an exhumed analogue of present-day plate boundary shear zones formed during the Early to Middle Miocene subduction of the Adria microplate beneath the frontal margin of the European plate (Vannucchi et al., 2008). The SVU appears as a map-scale tectonic mélange, about 200–500 m thick, comprising superposed lenticular tectonic slices separated by anastomosing shear surfaces (Remitti et al., 2013; Vannucchi et al., 2008). Its lithology consists mainly of shale and marl from the overthrusting accretionary complex (Ligurian and Subligurian Units) and associated slope deposits (Remitti et al., 2012; Vannucchi et al., 2008). Paleothermal indicators, such as vitrinite reflectance, clay-mineral geothermometers, and apatite fission track analysis (Botti et al., 2004; Carlini et al., 2013; Reutter et al., 1991; Thomson et al., 2010), suggest that sediments within the SVU and its footwall reached maximum temperatures of about 120–150°C, indicative of burial depths around 5 km. These values support the interpretation of the SVU as an equivalent to the shallower portion of modern seismogenic megathrusts (Mittempergher et al., 2018; Vannucchi et al., 2008).

Field observations reveal the progressive evolution of deformation during its activity, from early pre-litification deformation stage to brittle faulting (Cerchiari et al., 2020; Mittempergher et al., 2018). All deformation phases

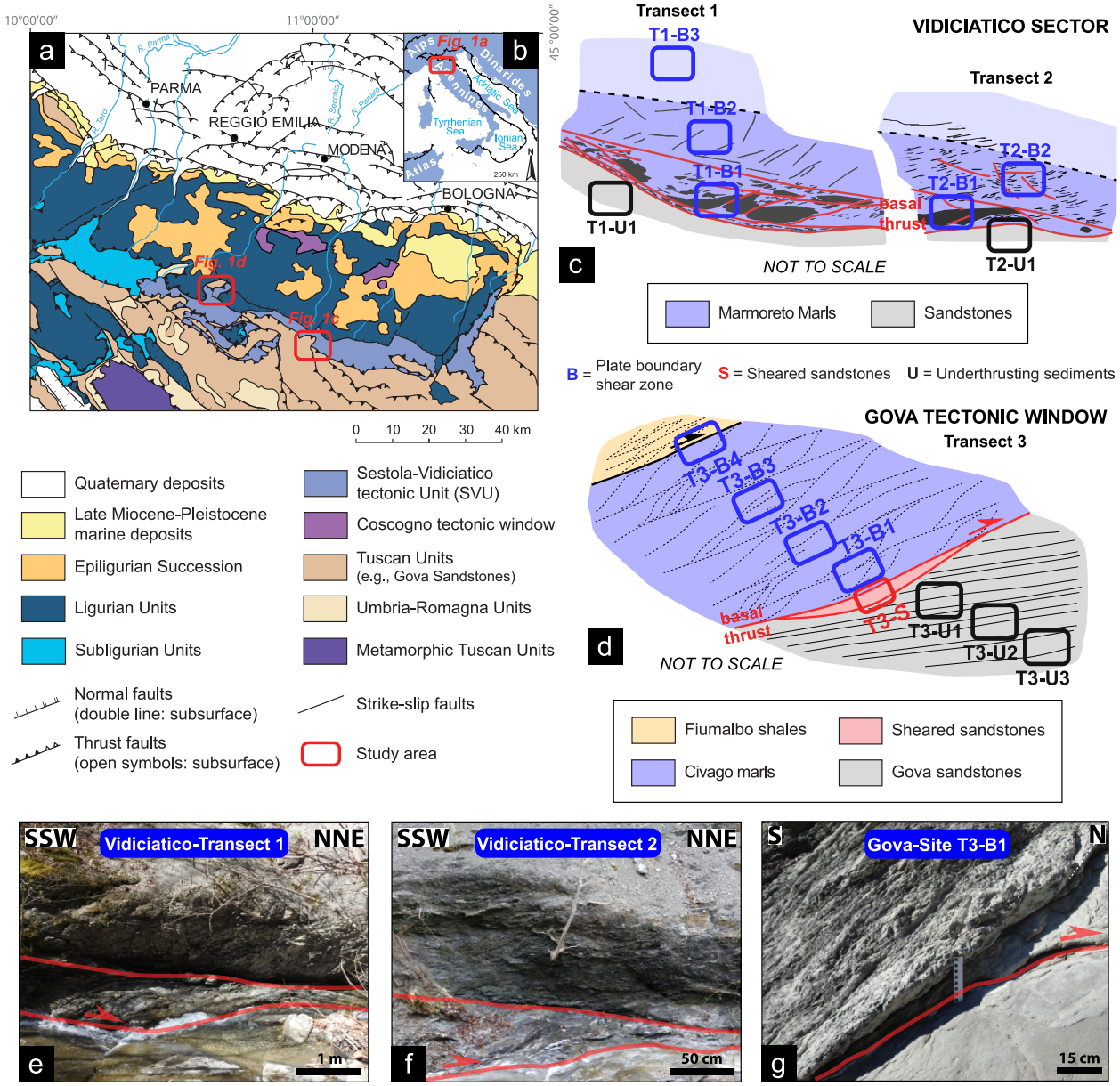

Figure 1. (a) Simplified structural map of the Northern Apennines (modified from Remitti et al. (2013)) and (b) its geographic location; sketches of the main structural features and the relative positions of the sampling-sites at (c) Vidiciatico (modified from Mittempergher et al., 2018) and (d) Gova (modified from Robustelli Test & Zanella, 2021); (e, f) detailed photos of the basal thrust of the SVU cropping out at Vidiciatico; (g) close-up of the basal décollement at Gova showing the contact between the Civago marls and the underlying sheared sandstones.

were coupled with circulation of considerable volumes of fluids. Integration with geochemical analyses of calcite veins provides insights into active fluid circulation, changes in fluid origins, and stress-regime variations during different phases of the seismic cycle. Particularly in the last brittle phase, crosscutting calcite veins along major faults and fractures reflect repeated faulting episodes driven by cyclical rises and drops in fluid pressure, stress-switching, and mineral precipitation (Cerchiari et al., 2020; Mittempergher et al., 2018; Vannucchi et al., 2008).

Stable isotope analyses ($\delta^{13}C$ and $\delta^{18}O$; see Vannucchi et al., 2010) of calcite veins and wall rocks suggest the likely influx of deep diagenetic fluids, possibly released by smectite dewatering at depth, buffered by the fault wall rocks. Geochemical (major and trace elements) analyses of veins in the basal thrust zone highlight fluid circulation and stress-switching during repeated seismic-cycles (Cerchiari et al., 2020). During the coseismic phase, exotic fluids under reducing condition, in disequilibrium with the wall rocks, migrated along the major

fault, followed by a switching in stress field. In the postseismic phase, extensional veins recorded circulation of local fluid equilibrated with the wall rock. These fluids were locally modified by sorption reactions and pressure-solution processes. Finally, during the reloading phase, fluid pressure increases, restoring the compressional regime.

3. Samples and Rock Magnetic Approaches

3.1. Samples Location and Characteristics

Sampling was conducted in two representative sectors exposing the basal thrust of the SVU (Figure 1), where its evolution is well-constrained by previous fieldwork and mesoscale structural studies (e.g., Mittempergher et al., 2018; Remitti et al., 2012; Vannucchi et al., 2008), paleothermal estimations (Carlini et al., 2013; Reutter et al., 1991), and geochemical analyses from calcite veins (Cerchiari et al., 2020; Vannucchi et al., 2010). Additionally, preliminary rock magnetic mineralogical experiments conducted at the same outcrops (Robustelli Test & Zanella, 2021) confirm the suitability of the magnetic properties of the sediments within the SVU to record variations in faulting processes.

Multiple hand-samples were collected from both the footwall and hangingwall of the basal thrust, separating the SVU from the underlying Adria sedimentary cover, along three transects perpendicular to the main thrust (Figures 1c and 1d). Each transect comprises multiple sites positioned at progressively increasing distances from the basal thrust. Site names include the transect number and an acronym indicating the structural position or origin of the tectonic slice (U = Underthrusting sediments; S = Sheared sandstones; B = SVU). Sites are further numbered according to their relative distance from the basal thrust (e.g., T1-B1, T1-B2 and T1-B3).

Two transects (Transects 1 and 2) were sampled at Vidiciatico (44°10′16.13″N–10°51′42.42″E, Figures 1a and 1c). In the hanging wall of the basal thrust, samples were taken from the marls of the prism slope incorporated within the SVU (e.g., Marmoreto Marls and/or Civago Marls; Plesi et al., 2002; Vannucchi et al., 2010), which are characterized by a penetrative fabric consisting of rhombohedral lithons separated by shear fractures and cut by localized shear zones subparallel to the main faults (Figures 1e and 1f). In the footwall, the collected samples consist of poorly deformed turbidites from the Umbrian-Tuscan sedimentary succession (Botti et al., 2011).

The third transect is located within the Gova tectonic window (44°20′12.08″N–10°31′37.99″E; Figures 1a and 1d). In the hanging wall of the basal thrust, samples were collected from the first tectonic slice of marls inside the SVU, characterized by a well-developed pressure-solution cleavage (Figure 1g), bounding rhombohedral to lens-shaped lithons. The pervasive tectonic fabric is cut by extensional veinlets associated with hydraulic fracturing (Remitti et al., 2012; Vannucchi et al., 2010). Additional samples were taken from a layer of sheared sandstones pinched along the basal thrust, demonstrating incomplete lithification of the foredeep turbidites during the early stages of thrust activity (Remitti et al., 2012). Finally, three sites at progressively increasing distance from the basal thrust were sampled from the undeformed turbiditic layers of the footwall (Gova sandstones; Cornamusini et al., 2018; Plesi, 2002).

3.2. Magnetic Mineralogy Investigation

Rock magnetic experiments were conducted to evaluate variations in magnetic mineral assemblages, concentration, and grain size induced by fluid-rock interaction with distance from the main thrusts. Bulk mass-normalized magnetic susceptibility (χ, units of m^3/kg) was measured with a KLY-3 Kappabridge (operating at 875 Hz and 300 A/m; AGICO) to provide information on the concentration of para-, dia- or ferri-magnetic minerals (Tarling & Hrouda, 1993; Thompson & Oldfield, 1986; see Text S1 in Supporting Information S1). Room temperature field- and frequency-dependence of magnetic susceptibility χ was measured at three operating frequencies (976, 3,904 and 15,616 Hz) as a function of field increase from 2 to 700 A/m, 2 to 350 A/m, and 2 to 200 A/m for each respective frequency, using a MFK2-FA (AGICO). The field dependence of magnetic susceptibility, expressed by the parameter V_a (details in Text S3 in Supporting Information S1), can be used to detect the presence of pyrrhotite and titanomagnetite (e.g., Hrouda et al., 2006; Jackson et al., 1998; Worm et al., 1993). Frequency-dependent magnetic susceptibility (χ_{fd}; Dearing et al., 1996; Text S2 in Supporting Information S1) was calculated to identify the contribution of SP particles over SD and MD grains (Dearing et al., 1996; Maher, 1988; Thompson & Oldfield, 1986; Text S2 in Supporting Information S1).

Natural remanent magnetization (NRM) was measured with a JR-6 spinner magnetometer, followed by stepwise static alternating field (AF) demagnetization steps up to 100 mT to identify the median destructive field (MDF), a proxy for coercivity (Text S3 in Supporting Information S1). To define variations in ferrimagnetic mineral (e.g., magnetite) concentrations, anhysteretic remanent magnetization (ARM) was imparted at 100 mT with a bias direct field of 0.1 mT. AF demagnetization of ARM and IRM imparted at 100 mT was performed to further constrain the grain size and genesis of magnetic mineral assemblages. On selected specimens from each site, isothermal remanent magnetization (IRM) acquisition curves were obtained using a pulse magnetizer at progressively increasing field steps up to a saturation remanent magnetization (SIRM) of 1.5 T. Backfield remanent curves were measured to detect the coercivity of remanence (B_{cr}; Text S3 in Supporting Information S1) by applying progressively increasing backfields up to −0.3 T. Log-normal probability density functions (PDFs) were fitted to the gradient of the acquisition data and evaluated against the corresponding cumulative distribution functions (CDFs) using the Bilardello (2025) CoercivityUnmixing code, which includes residual analysis and component intersection detection to discriminate magnetic components, their mean remanent coercivity (Bh) and dispersion parameter (DP) (Heslop et al., 2002; Kruiver et al., 2001; Text S3 in Supporting Information S1; Table S1). The remanence curves were also used to calculate remanence ratios (S-ratios, Thompson & Oldfield, 1986; HIRM, Robinson, 1986; L-ratio, Liu et al., 2007; Table S2) using the SIRM and backfield IRMs at 100 and 300 mT to evaluate the relative contributions of high- and low-coercivity phases (King & Channell, 1991; Liu et al., 2019; Text S3 in Supporting Information S1).

Hysteresis loops were acquired at room temperature using a vibrating sample magnetometer (VSM, Lake Shore 7410 at the INRiM, Italy, and Lake Shore 8600 at the IRM) with a maximum applied field $B_{max} = 1.5$ T, to further investigate the rock magnetic properties and estimate the magnetic domain-state (i.e., grain size of magnetic minerals) (Day et al., 1977; Dunlop, 2002a, 2002b). The high-field magnetic susceptibility (χ_{hf}; defined by the slope of the hysteresis loops above 700 mT) and the "ferrimagnetic susceptibility" ($\chi_{ferri} = \chi - \chi_{hf}$; Text S1 in Supporting Information S1) are used as proxies for the contributions of dia-/para-magnetic and ferrimagnetic minerals to the bulk susceptibility, respectively. Ferrimagnetic susceptibility is used to normalize grain-size and field- and frequency dependent parameters (see Text S2 and S3 in Supporting Information S1) to correct for the paramagnetic clay minerals contribution (e.g., $\chi_{fd\text{-}normalized}$, Dearing et al., 1996; Maxbauer et al., 2016a; Yamazaki & Ioka, 1997). Additional hysteresis cycles at room temperature were measured after thermal treatments under vacuum at increasing maximum temperatures between 150 and 650°C in 100°C steps to assess changes in the magnetic properties with increasing temperature. Each thermal treatment was performed, by heating the samples for 1 hr with a vacuum furnace. Interpretation of hysteresis loops was performed with the HystLab software (Paterson et al., 2018). Advanced processing options (e.g., automatic loop centering, drift and high-field slope corrections, and loop fitting) were applied following the approach described by Paterson et al. (2018) and Jackson and Solheid (2010). Only hysteresis loops with raw loop quality factor $Q > 2$ and ferromagnetic loop factor Qf > 1 were considered reliable for calculating hysteresis parameters. Saturation magnetization (M_s), saturation remanent magnetization (M_{rs}) and coercivity (B_c) were extracted and plotted as M_{rs}/M_s versus B_{cr}/B_c (i.e., Day plot; Day et al., 1977; Dunlop, 2002a, 2002b), allowing estimation of the domain-state. Hysteresis ratios were used to calculate the D_{JH} ratio (see Table S2 and Text S3 in Supporting Information S1) to identify the occurrence of iron sulfides (Housen & Musgrave, 1996). First-Order Reversal Curves (FORC) were also measured on selected samples and processed using the VARIFORC software (Egli, 2013, 2023).

Low-temperature measurements were conducted using a Quantum Designs Magnetic Properties Measurement System (MPMS-XL) at the Institute for Rock Magnetism (IRM) at the University of Minnesota. Field cooled (FC) remanence experiments were performed by applying a 2.5 T field while cooling the specimens from 300 to 10 K and measuring the magnetic remanence as the specimens warmed back to 300 K (in zero field). After cooling the specimens to 10 K in zero field, a low-temperature SIRM (LT-SIRM) at 2.5 T was imparted. The remanence was subsequently measured while warming up to room temperature in zero field (i.e., zero-field cooled (ZFC) remanence). Finally, a SIRM of 2.5 T was imparted at room temperature (RT-SIRM at 300 K) and the remanence was measured during a cooling-warming cycle (300–10–300 K) in zero field. This procedure is particularly suitable for identifying diagnostic magnetic phase transitions indicative of magnetite (Verwey transition, T_V ~120 K; Verwey, 1939; Muxworthy & McClelland, 2000), hematite (Morin transition, T_M ~260 K; Morin, 1950; Özdemir et al., 2008), or monoclinic pyrrhotite (Besnus transition, T_B ~34 K; Dekkers, 1989; Rochette et al., 1990). Additional information on magnetic particle grain size or concentration can be assessed trough

several parameters (δ_{FC}/δ_{ZFC}, Carter-Stiglitz et al., 2004; Moskowitz et al., 1993; R_{LT}, Smirnov, 2009; PM_{ZFC}, Aubourg & Pozzi, 2010; Memory Ratio, Dunlop & Argyle, 1991; RI ratio, Dekkers, 1989; Liu et al., 2006; G%, Aubourg et al., 2021; see details in Text S1–S3 of Supporting Information S1 and Table S1).

Stepwise thermomagnetic susceptibility (χ–T) curves were acquired in argon during heating-cooling cycles to successive elevated temperatures (increments of 50°C from 150 to 350°C and then 700°C) using a KLY-2 Kappabridge equipped with a CS2 furnace at IRM (University of Minnesota). Stepwise χ–T is used to determine the Curie/Néel temperatures of the magnetic minerals in our samples and to quantify thermochemical alteration during heating (alteration indexes, A_{40}, δ_χ, A_m, and δ_{cr}; Table S2; Text S4 in Supporting Information S1). Alteration temperatures can inform about the presence of thermally unstable magnetic minerals such as pyrite and goethite (Özdemir & Dunlop, 2000; Spassov & Hus, 2006; Yang et al., 2018) and/or potentially be used as a paleo/geothermometer (Hrouda et al., 2003; Spassov & Hus, 2006; Yang, Dekkers, & Zhang, 2016).

3.3. Scanning Electron Microscopy

Scanning electron microscope (SEM) observations, coupled with energy-dispersive spectrometry (EDS) measurements, were performed on thin sections from selected sites, including both the footwall and hangingwall, and at different distances from the basal thrust. Microprobe analyses were acquired using a SEM JEOL IT300LV, EDS Oxford Instruments Inca Energy 200, X-act SDD detector. For this kind of detector, the Aztec Energy version 6.0 SP1 provided with Oxford Instruments Aztec Feature ® package was used. Operating conditions are 15 keV with 5 nA current and EDS process time of 1 μsec, 10^5 counts/sec, and a live time of 50 s. Multispectral image analysis was performed on representative samples in SEM-EDS using the package Feature of the software Aztec. The analytical conditions for the multispectral images were as follows: accelerating voltage = 15 kV, probe current = 2 nA, working distance = 10 mm, LiveTime (LT) = 3 s. Thresholds were automatically established after visual inspection of back scattered electron (BSE) photomosaics.

The obtained elemental analyses were used to semi-quantitatively assess the composition of different mineralogical phases, with a particular focus on iron sulfides and total iron content.

4. Results

4.1. Magnetic Mineralogy (Assemblages, Concentration, and Domain States)

Marls from the hangingwall and sandstones of the footwall are characterized by bulk susceptibility (χ and χ_{hf}) values comprised between 3.75 and 13.00 × 10^{-8} m^3/kg (Table S3; Figure 2 and Figure S1 in Supporting Information S1), with values mainly controlled by the paramagnetic contribution (mean χ_{hf}/χ about 92% and 83%, respectively). Ferromagnetic s.l. phases occur in low amounts, as indicated by concentration proxies (e.g., $\chi_{ferri} < 4.10 \times 10^{-8}$ m^3/kg, NRM < 34.18 × 10^{-8} Am^2/kg and $M_s = 6.25 \pm 4.63 \times 10^{-4}$ Am^2/kg; Figure 2 and Figure S1 in Supporting Information S1; Table S3). ARM and SIRM values vary among lithologies, being lower in sandstones (Figure 2; Table S3).

Hysteresis loops at room temperature display a predominant paramagnetic behavior (Figure S4c in Supporting Information S1), with the ferrimagnetic component insufficient to define reliable hysteresis parameters in some samples. Hysteresis curves saturate between 0.3 and 0.6 T, with a narrow shape indicative of low-coercivity phases such as (titano-)magnetite. Only a few Marmoreto marls samples (T1-B3 in Figure S4c in Supporting Information S1) show wider loops with wasp-waisted shape, reflecting a mixture of low- and high-coercivity phases (Roberts et al., 1995).

The saturation ratio $S_{0.3}$ (~0.90 ± 0.12; Table S5) and coercivity analyses (Figures S5 and S6 in Supporting Information S1) indicate that remanent magnetizations are dominated by minerals with coercivities <0.3 T (e.g., titano-magnetites), with the high-coercivity fraction (>0.3 T) < 20% in most samples. Coercivity analysis (Figures S5–S7a in Supporting Information S1) reveals two dominant low-coercivity components: (a) a minor soft/low-coercivity phase ($B_{soft} = 17 \pm 9\%$; Bh = 1.29 ± 0.05 $\log_{10}$ units; DP = 0.30 ± 0.05) with values typical of detrital (titano-)magnetite (Egli, 2004a; Xue et al., 2024); (b) a dominant intermediate-coercivity component ($B_{inter} = 73 \pm 11\%$; Bh = 1.77 ± 0.05 $\log_{10}$ units; DP = 0.26 ± 0.03), likely representing the superposition of biogenic soft and biogenic hard components, as inferred from ARM coercivity analysis (Figures S7a and S8d in Supporting Information S1; Egli, 2004a; Kruiver et al., 2001; Maxbauer et al., 2016b). $V_{a\text{-normalized}}$ values (3%–

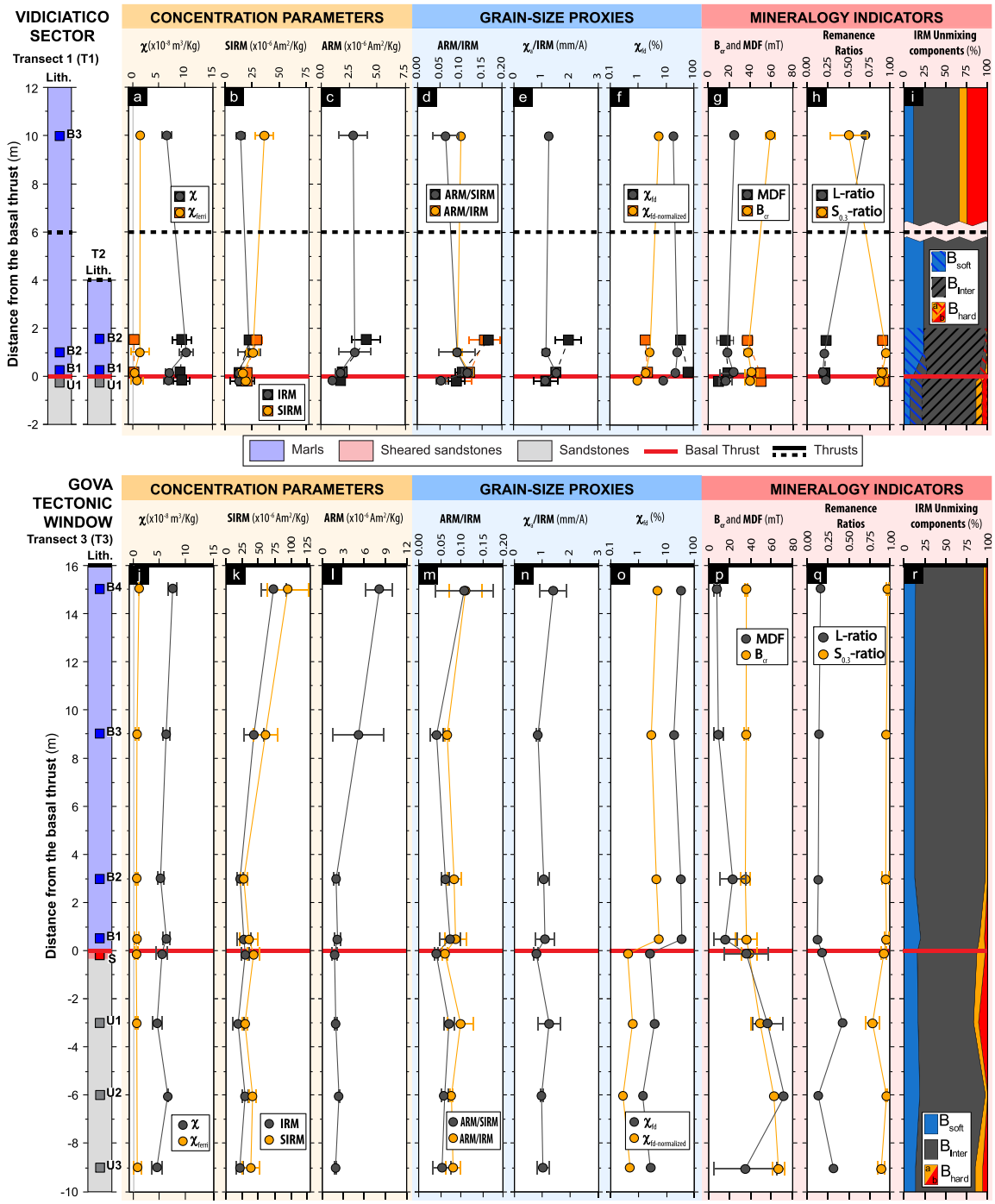

Figure 2. Plots of representative rock-magnetic parameters versus distance from the main thrust plane (a–i) at Vidiciatico and (j–r) Gova. Squares connected by dotted lines (a–h) refer to data from Vidiciatico Transect 2. See details in Figures S1–S3 of Supporting Information S1. (a, j) Magnetic susceptibility (χ) in gray and "ferrimagnetic susceptibility" (χ_{ferri}) in orange; (b, k) saturation isothermal remanent magnetization (SIRM) in orange and IRM imparted at 100 mT in gray; (c, l) anhysteretic remanent magnetization (ARM); (d, m) ARM/SIRM ratio in gray and ARM/IRM ratio in orange; (e, n) χ_a/IRM ratio; (f, o) frequency-dependent magnetic susceptibility (χ_{fd}) in gray and $\chi_{fd\text{-}normalized}$ in orange; (g, p) coercivity of remanence (B_{cr}) in orange and median destructive field (MDF) in gray; (h, q) L-ratio in gray and S-ratio $S_{0.3}$ in orange; (i, r) stacked area chart of relative contributions [%] of the magnetic components unmixed from the IRM; B_{soft}, B_{inter}, and B_{hard} correspond to the low-, intermediate- and high-coercivity component, respectively.

44%) support varying amounts of titano-magnetite (Hrouda et al., 2006), being higher in Vidiciatico Transect 2 (Figure S3d in Supporting Information S1). Overall, Ti-content varies between pure magnetite to relatively Ti-rich magnetite (Figure S9b in Supporting Information S1). Mineral-diagnostic plots (Figures S7b and S7c in

Supporting Information S1) confirm a dominant (titano-)magnetite assemblage, with local occurrence of greigite in few samples, particularly in the lower plate sandstones.

Significant content of high-coercivity minerals is observed in sandstones (HIRM = 53.50 ± 21.77 A/m, L-ratio = 0.25 ± 0.14) and Site T1-B3 (L-ratio = 0.70; $S_{0.3}$ = 0.51).

Coercivity analysis (Figures S5–S7a in Supporting Information S1) reveal two distinct high-coercivity components with values typical of hematite or goethite: (a) a first hard/high-coercivity phase (B_{hard}a; Bh = 2.42 ± 0.15 $\log_{10}$ units; DP = 0.19 ± 0.04); (b) a second hard component with distinct higher coercivity (B_{hard}b; Bh = 3.12 ± 0.13 $\log_{10}$ units; DP = 0.15 ± 0.05). The 1.5 T maximum field used for coercivity analysis is likely insufficient to fully capture the median field of the highest-coercivity component, which appears to be larger, suggesting goethite (e.g., Figure S5 in Supporting Information S1).

Hysteresis parameters (M_{rs}/M_s = 0.12 ± 0.07) are characteristic of pseudo single domain (PSD) or vortex state magnetite grains (Dunlop, 2002a). Typical PSD values are determined by grain-size parameters (Table S4), such as SIRM/χ_{ferri} = 5.81 ± 3.11 kA/m, ARM/χ_{ferri} = 0.49 ± 0.40 kA/m, and ARM/IRM = 0.10 ± 0.03. These parameters tend to be higher in marls compared to sandstones and vary according to structural position (Figure 2 and Figure S2 in Supporting Information S1).

In contrast, most samples show χ_a/IRM > 1 mm/A (Table S4) and easier demagnetization of IRM curves with MDF_{ARM}/MDF_{IRM} ratios >1 (Figure S8 in Supporting Information S1), suggesting significant contribution of SD magnetite grains (Egli & Lowrie, 2002; Xu & Dunlop, 1995). However, low D_{JH} values (<0.12) exclude the dominance of high-coercivity SD iron sulfides (e.g., greigite and pyrrhotite; Housen & Musgrave, 1996).

Diagrams of stacked FORC measurements (Figure S9a in Supporting Information S1), although somewhat noisy, display an asymmetrical triangular contour shape spreading along the B_u axis with a central peak reaching B_c around 80–100 mT, consistent with mixed PSD-SD magnetite grains (Egli, 2021; Muxworthy & Dunlop, 2002; Roberts et al., 1995).

Frequency-dependent magnetic susceptibility varies between lithologies. χ_{fd} and $\chi_{fd\text{-}normalized}$ are <6% in sandstones (Table S4; Figure 2 and Figure S3 in Supporting Information S1), excluding dominance of SP particles (Maxbauer et al., 2016a) or pyrrhotite (Worm et al., 1993). However, in marls, elevated $\chi_{fd\text{-}normalized}$ (13.12 ± 14.91%) along with variations in χ_{erri}/M_s indicate the local occurrence of SP magnetite grains.

4.2. Low-Temperature Experiments

The FC and ZFC remanence curves display decay of remanence upon warming (Figures 3a and 4a). FC curves exhibit higher magnetization than ZFC, both converging at ~250–300 K, suggesting the occurrence of goethite (Liu et al., 2006). Most samples show a drop at ~124 K, consistent with the Verwey transition (T_v) of magnetite (Muxworthy & McClelland, 2000; Verwey, 1939). The absence of a clear T_v in some samples (Figures 3a and 4a) is indirect evidence of the presence of Ti-magnetite and/or more oxidized magnetite/maghemite (Chang et al., 2013). The remanence loss across the Verwey transition (δ; see Figure S10 in Supporting Information S1 and Table S5) is <0.8 for δ_{FC} and <0.4 for δ_{ZFC}, with variations with structural position.

The values of low-temperature remanence ratios (δ_{FC}/δ_{ZFC} = 1.71 ± 0.55; R_{LT} = 2.31 ± 1.01; Figure S10 in Supporting Information S1; Table S5) support the occurrence of significant SD contributions mixed with PSD magnetite grains (Housen & Moskowitz, 2006; Smirnov, 2009). In marls, variations are observed according to distance from the basal décollement, with R_{LT} markedly varying between 1.18 and 4.37, confirming the presence of SD to PSD magnetite mixtures and goethite (Jackson et al., 2011; Smirnov, 2009).

The remanence loss between 10 and 35 K differs among lithologies, with values about 0.48 ± 0.05 in sandstones and 0.65 ± 0.13 in marls (Figure S10 in Supporting Information S1; Table S5). Overall, mean PM_{ZFC} values of about 0.61 and the absence of a Besnus transition preclude the presence of pyrrhotite (Aubourg & Pozzi, 2010).

The RT-SIRM cooling curves (Figures 3b and 4b) show an initial gradual increase in magnetization, followed by a faint to well-developed loss at ~120 K, then a continuous increase down to 10 K. Sheared sandstones at Gova show two drops in the cooling curves at 126 and 247 K, consistent with the Verwey and Morin transition, respectively (Figure 4b). A similar trend is observed in the footwall at Vidiciatico (Figure 3b). Upon warming, the remanence is not completely recovered passing through the Verwey transition, with a remanence loss of about

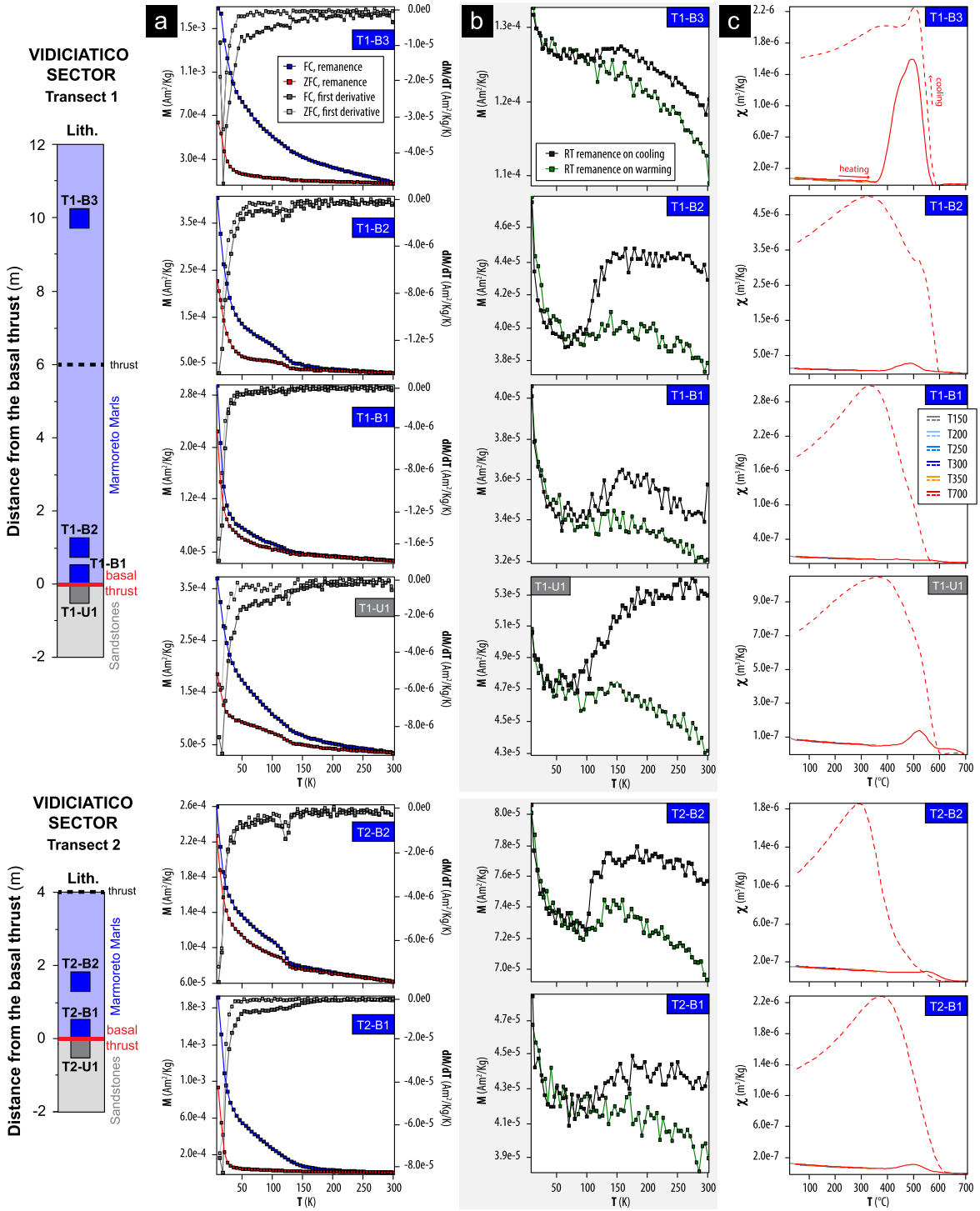

Figure 3. (a) Representatives FC-ZFC (blue and red, respectively) with first derivatives (dark and light gray, respectively), (b) RT-SIRM remanence (black/green are cooling/warming data, respectively), and (c) stepwise thermomagnetic susceptibility curves (solid/dotted are heating/cooling curves, respectively; details in Figure S11 of Supporting Information S1) from the Vidiciatico Sector (Transect 1 and 2). Lithological units and relative position of the samples are reported on the left.

8%–19% (Memory ratio = 0.88 ± 0.04; Figure S10 in Supporting Information S1 and Table S5), followed by a monotonic decrease from 120 to 300 K. The remanent magnetization on cooling generally increases by >7%, indicating that goethite constitutes an appreciable portion of the SIRM (Dekkers, 1989). Marls show increases in magnetization of ∼14 ± 8%, while some sandstones also exhibit a significant SIRM loss during cooling to 10 K

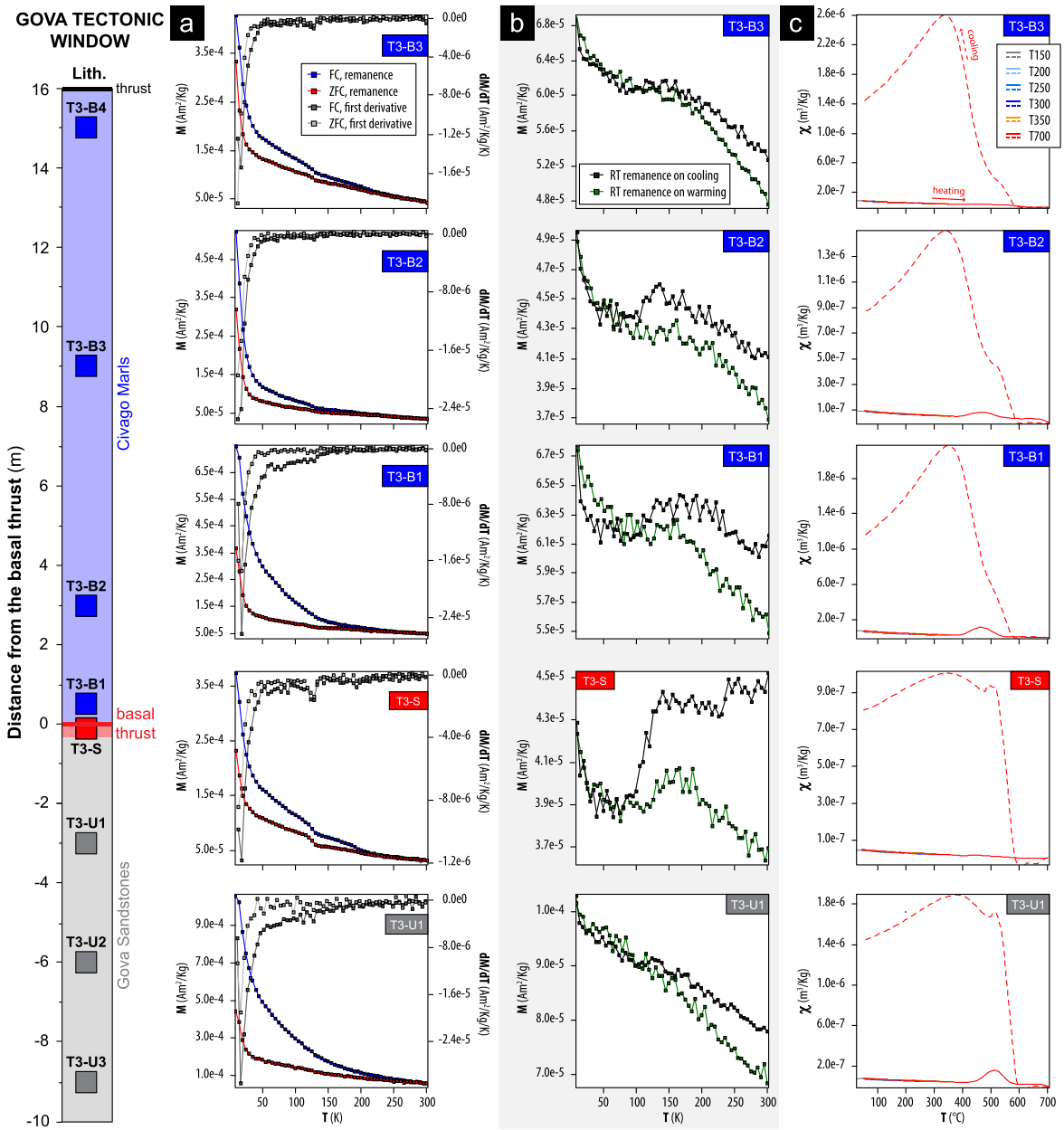

Figure 4. (a) Representatives FC-ZFC with first derivative, (b) RT-SIRM remanence, and (c) stepwise thermomagnetic susceptibility curves from the Gova Tectonic Window (see Figure S12 in Supporting Information S1 for details). Details as in the caption of Figure 3.

(Figures 3b and 4b). At Vidiciatico, the magnetization increases are generally less intense, with higher values (~10%) at sites T1-B1 and T2-B1 (Figure 3b and Figure S10f in Supporting Information S1). At Gova (Figure 4b), some samples show a monotonic increase in magnetization and a faint inflection close to the T_v with magnetization increases >30% in the footwall and at site T3-B3 (Figure 4b; Table S5). The goethite proxy (G%; Aubourg et al., 2021) is significantly higher at Gova, ranging from 4% to 20%. In contrast, at Vidiciatico, G% is typically <11% (Figure S10 in Supporting Information S1; Table S5).

4.3. High-Temperature Experiments

The stepwise χ–T cycles are almost reversible and exhibit a paramagnetic hyperbolic behavior up to a maximum temperature of 350–450°C (Figures 3c and 4c, Figures S11a and S12a in Supporting Information S1), suggesting negligible alteration (alteration indices <10%; A_{40}, δ_χ, A_m, and δ_{cr}; Table S7 in Supporting Information S1) at

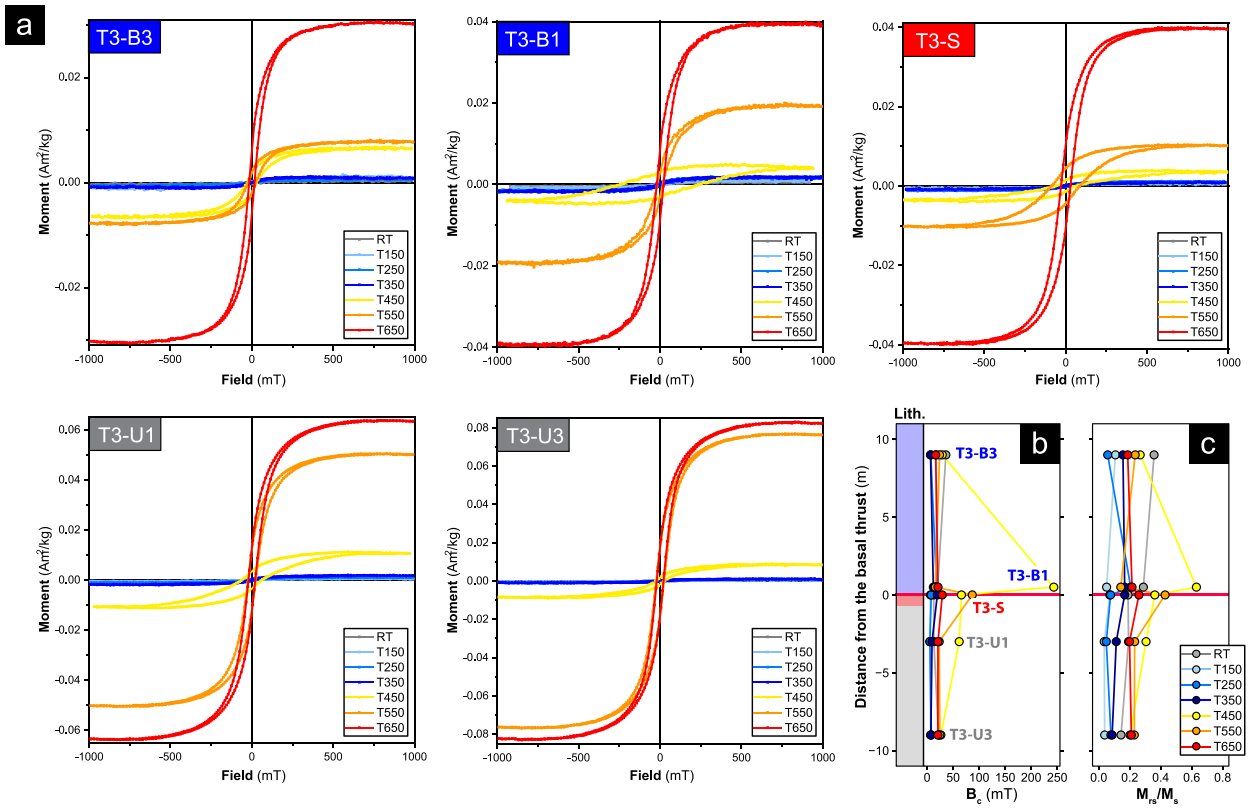

Figure 5. (a) Hysteresis loops after stepwise thermal treatment. Loops are corrected for the high-field slope. Raw data are reported in Figure S13 of Supporting Information S1. Hysteresis paramenters (b) B_c and (c) M_{rs}/M_s versus distance from the basal décollement. Lithological units are also reported. See Figure 1 for samples position.

these temperatures. Suceptibility starts to increase above ~350°C and reaches maximum values between 500 and 550°C, suggesting the thermal decomposition/breakdown of iron-bearing paramagnetic minerals, such as pyrite and/or clays and neoformation of ferrimagnetic minerals (e.g., magnetite; Tanikawa et al., 2008; Yang, Dekkers, & Zhang, 2016). Only a few marl samples start to alter at about 350°C (T1-B3 in Figure S11 of Supporting Information S1 and T3-B1 in Figure S12 of Supporting Information S1), showing A_{40} and δ_χ = 17%–22%, A_m = 12%–19%, and δ_{cr} = 19%–31%. In most samples, χ becomes nearly zero at about 600°C, indicating the presence and/or neoformation of magnetite. Some specimens show a significant loss of χ at 580–600°C but reaches zero at 700°C, suggesting the local occurrence of hematite (e.g., T3-U1 in Figure S12 of Supporting Information S1); however, this might be a product of thermal alteration.

Overall, the heating-cooling cycles to 700°C show irreversible curves with abrupt increases in χ upon cooling, suggesting significant neoformation of magnetite during the thermal treatment.

Different behaviors are observed in the cooling curves depending on the lithology: In sandstones, χ increases sharply at 580–600°C to an order of magnitude higher, followed by a slight increase, reaching maximum values at 350–400°C (e.g., Figure 4c); Marls display an initial rapid increase in susceptibility between 580 and 550°C, followed by a monotonic increase with decreasing temperature, with a peak between 300 and 350°C (Figures 3c and 4c).

Hysteresis loops after stepwise thermal treatments (Figure 5a) reveal low saturation magnetization (M_s) up to 350°C with values $< 1.84 \times 10^{-3}$ Am^2/kg. At low temperature steps, the signal is dominated by paramagnetic behavior, with slight increases in M_s from T_{max} = 250°C (Figure S13 in Supporting Information S1). Hysteresis parameters (M_s, B_c, and M_{rs}/M_s) significantly increases after the 450°C step (Figure 5). Overall, the M_s values after the 650°C step are two orders of magnitude higher than the initial values (Figure 5a). At the 650°C thermal step, the hysteresis loops show a pot-bellied shape (shape parameter $\delta_{hyst} < 0$) and are characterized by

B_c < 30 mT, supporting the neoformation of low-coercivity ferrimagnetic minerals (e.g., magnetite) as the final alteration product of paramagnetic minerals.

The intensity of alteration and intermediate products differs between lithologies and with distance from the main thrust plane (Figure 5).

In the footwall, the hysteresis loops widen at 450°C with changes in B_c from <10 to 27 mT and 62 mT at site T3-U3 and T3-U1, respectively. M_s increases significantly after the 550°C step, reaching maximum values of 8.28×10^{-2} Am^2/kg. The sheared sandstones, closer to the main thrust, show higher B_c value of 87 mT at the 550°C step (Figure 5b). M_s increases sharply only after the final thermal step, and the hysteresis loop shape transitions from wasp-waisted ($\delta_{hyst} \sim 1$) to pot-bellied (δ_{hyst} about −0.1; Figure 5a).

In the marls, at greater distance from the basal thrust (Site T3-B3), hysteresis loops support progressive magnetite formation after the 350°C step with significant increase during the final thermal step. The hysteresis loop shape is initially wasp-waisted ($\delta_{hyst} > 0.5$) but becomes pot-bellied at the 650°C thermal step (Figure 5a). In contrast, closer to the basal thrust, at the 450°C step, B_c reaches 243 mT and M_{rs}/M_s ratio attains its highest value of 0.63 (Figures 5b and 5c), suggesting the neoformation of high-coercivity minerals such as hematite (Özdemir & Dunlop, 2014) as an intermediate product.

4.4. Scanning Electron Microscopy

Petrographic observations performed using SEM-EDS analysis reveal the presence of pyrite microcrysts (FeS_2) while no direct evidence of greigite were observed (Figure 6). In the marls of the SVU hanging wall, pyrite occurs either as isolated crystals (1–10 μm in diameter) or as large aggregates of framboids (~150–300 μm; Figures 6a and 6b, and Figure S14a in Supporting Information S1). At the tips of the aggregates, smaller framboids are distributed along dissolution seams, forming shadow-like micro-pyrite tails (Figure 6a) or bounding deformed domains (Figure S14d in Supporting Information S1). Large aggregates show alteration/recristallization rims with minor abundance of framboids or their relicts (Figures S14a and S14d in Supporting Information S1). Elongated pyrite inclusions are observed within deformed phyllosilicates (Figure S14e in Supporting Information S1).

In contrast, within the sandstones, pyrite framboids are typically isolated and dispersed between clays or within the carbonate matrix and preserved bioclasts. These framboids show no preferred orientation or specific spatial distribution (Figures 6c and 6d).

Overall, pyrite is more abundant close to the basal thrust, while Fe content varies among lithologies and depending on structural position (Figures 6f and 6g).

5. Discussion

This section discusses the distribution of magnetic mineral assemblages, their grain size, and concentration within the wall rocks relative to the major thrusts. The data set is compared with those from shear zones exhibiting evidence of frictional heating. Finally, a correlation is proposed between rock magnetic evidence and fluid- and stress-regimes to elucidate migration pathways, redox-conditions, and fluid-rock interactions during the seismic cycle.

5.1. Magnetic Minerals Distribution Across the SVU Megathrust

The magnetic mineral assemblages across the three transects consist of dominant paramagnetic clays and pyrite, as indicated by low magnetic susceptibility ($\chi < 10 \times 10^{-8}$ m^3/kg), χ-T cycles, hysteresis loops, and SEM-EDS analysis. A significant proportion of low-coercivity ferrimagnetic minerals (e.g., titano-magnetite) is present, along with minor amounts of high-coercivity phases, such as hematite and goethite. Variations in magnetic mineral distributions correlate with lithological unit and structural position.

In the hangingwall of the basal thrust, (titano-)magnetites are the dominant ferromagnetic s.l. phases, as indicated by high $S_{0.3}$, low B_{cr}, HIRM, and L-ratio values, with a complex primary mixture of likely biogenic ($B_{inter} \sim 70\%$) and detrital (B_{soft}) magnetite combined with titano-magnetites or slightly oxidized phases (Figure 2 and Figure S3 in Supporting Information S1). The Marmoreto Marls of Vidiciatico likely contain higher content of titano-magnetites and/or strongly oxidized magnetite or maghemite, as indicated by the absence of a discernible T_v

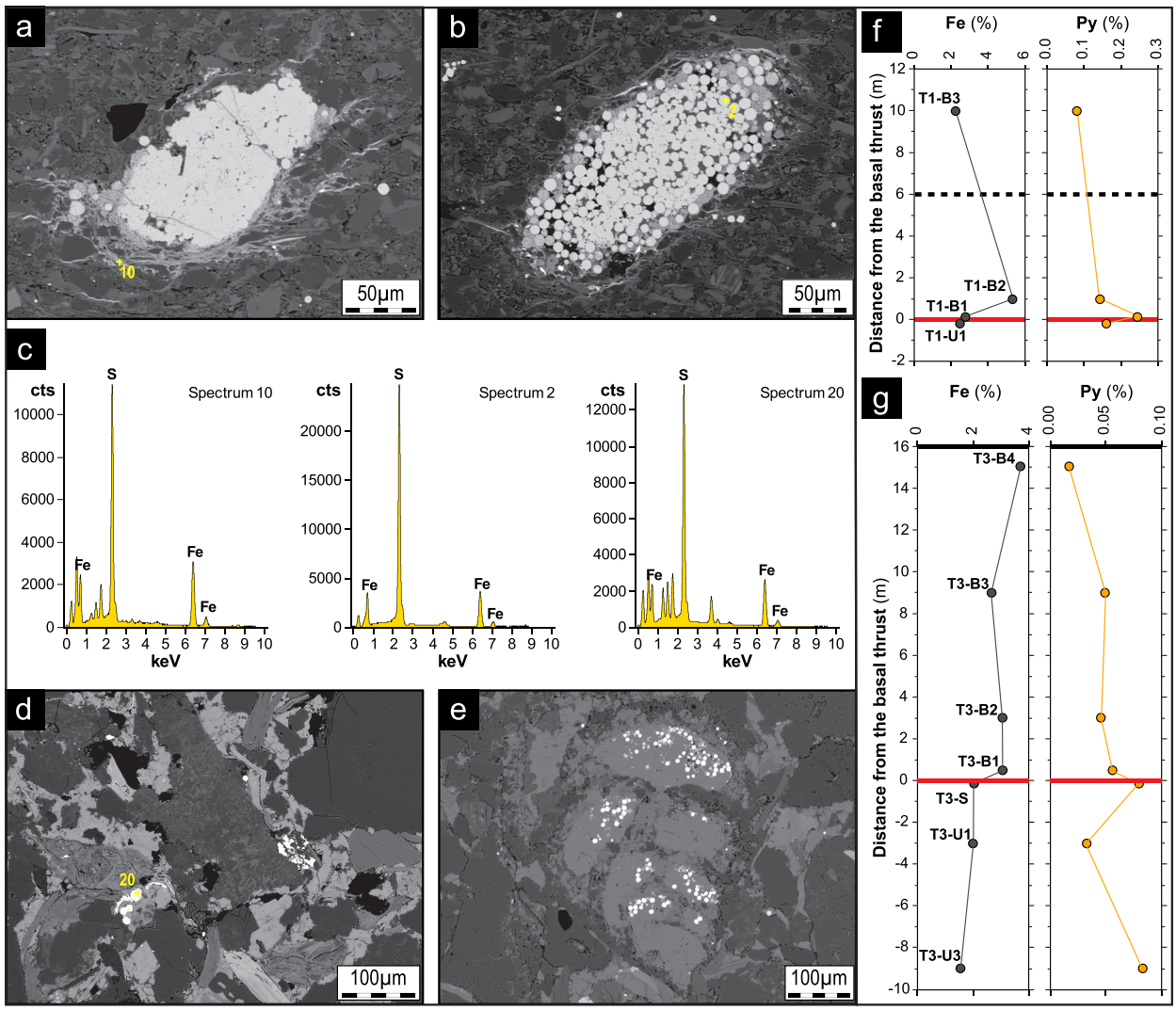

Figure 6. Backscattered SEM image of: (a, b) large aggregates of framboidal pyrite within the SVU marly domains; isolated framboids in the foredeep turbidites (d, e). (c) Representative EDS spectrum of pyrite microcrysts and framboids. Plots of relative abundance of Fe and pyrite content versus distance from the main thrust plane (f) at Vidiciatico and (g) Gova.

(Chang et al., 2013, Figures 3a), a relative increase in $V_{\text{a-normalized}}$ (particularly at Vidiciatico Transect 2) and an RI ratio ~10%, with higher oxidation near the basal décollement (Figure 3b and Figure S10f in Supporting Information S1).

Concentration trends vary depending on structural position, with minor variations between the two localities. At Vidiciatico, decreasing χ and Fe content corresponds to decrease in iron-oxides and Fe-bearing paramagnetic minerals close to the main thrust surface (Figures 2a and 6f). Conversely, χ at Gova, and thus the relative concentration of Fe-bearing minerals, is minimum at 3 m from the thrust and increases approaching the major fault surfaces (Figure 2j). Across all transects, the progressive decreases in χ_{hf} and alteration indices (Figure S1 and Table S7 in Supporting Information S1) near the basal décollement suggest potential Fe^{2+} depletion from Fe-bearing clays and/or pyrite dissolution (Hashimoto & Kaji, 2012; Yang, Dekkers, & Zhang, 2016), compatible with alteration rims in pyrite large framboids (Figure S14 in Supporting Information S1).

Magnetite concentration increases with distance from basal décollement, as evidenced by increasing ARM, SIRM, NRM, Fe content, and χ_{ferri} values upward in the hangingwall (Figure 2 and Figure S1 in Supporting Information S1).

χ_a/IRM, MDF_{ARM}/MDF_{IRM}, δ_{FC}/δ_{ZFC} ratios >1 and high memory ratio values indicate a significant contribution of SD (titano-)magnetite mixed to PSD grains (Dunlop & Argyle, 1991; Egli & Lowrie, 2002; Housen & Moskowitz, 2006), with grain-size variations depending on structural position. Overall, increasing SIRM/χ_{ferri}, ARM/χ_{ferri}, ARM/IRM, χ_a/IRM, and MDF_{ARM}/MDF_{IRM} support a main trend of relative enrichment in fine-grained (titano-)magnetite with distance from basal décollement (Figure 2 and Figure S2 in Supporting Information S1). Minimum values are observed in the central portion of the tectonic slices (around 2–4 m from the main thrust, whereas a secondary relative enrichment in SD grains can be identified along the main thrust (first 50 cm, e.g. Site T1-B1 Figure 2 and Figure S2 in Supporting Information S1) from a slight to significant increase in grain-size proxies.

In addition, at both Gova and Vidiciatico Transect 2, localized enrichment in fine-grained magnetite close to the SP-SD transition near the basal thrust is indicated by increased χ_{fd} (as χ_{fd} ~6%; $\chi_{fd\text{-}normalized}$ > 30%; Dearing et al., 1996; Maxbauer et al., 2016a) and χ_{ferri}/M_s coupled with higher δ_{FC}/δ_{ZFC} and R_{LT} (e.g., Site T3-B1 in Figure 2, Figures S2 and S10 of Supporting Information S1). At Vidiciatico Transect 2, the significant localized enrichment of magnetite nanoparticles near the basal thrust, also reflected by increased PM_{ZFC} and pronounced remanence loss (Site T2-B1 Figure 3a and Figure S10 in Supporting Information S1), may explain the low ARM/χ_{ferri} and ARM/IRM values.

High-coercivity minerals occur as accessory minerals (B_{hard} ~ 3–10%) with relative enrichment close to the main thrust (first meter upward; Figure 2 and Figure S3 in Supporting Information S1). An exception is represented by Site T1-B3 at Vidiciatico, where B_{hard} constitutes 34% of the total IRM. Low-temperature measurements (e.g., G% and FC-ZFC curve-spacing; Figures 3 and 4 and Figure S10 in Supporting Information S1) and high L-ratio (~0.7), and HIRM (>70 A/m) confirm significant goethite content, which may have formed due to interactions with hotter coseismic fluids (Chou et al., 2012).

Notable differences exhist between the two localities. For example, at Gova, higher R_{LT} and G% support higher goethite content than at Vidiciatico. Curvature variations in FC curves and the temperature at which they converge with ZFC curves (Figures 3 and 4) suggest different goethite grain sizes (Guyodo et al., 2003), with nano- and micro-goethite at Gova and Vidiciatico Transect 1, respectively. Additionally, at Gova, a high RI of 31% supports the presence of "pure" goethite (absent/limited substitutions; Dekkers, 1989; Kars et al., 2015). Overall, G% decreases closer to the basal décollement suggest upward relative enrichment of goethite in the hangingwall. In addition, at Gova and Vidiciatico Transect 2, proxies such as FC-ZFC curve-spacing, δ_{FC}/δ_{ZFC}, and R_{LT} indicate a goethite enrichment also close to the basal décollement (Figures 3 and 4 and Figure S10 in Supporting Information S1).

The sheared sandstones, just below the basal thrust at Gova, exhibit lower content in both para- and fine-grained ferrimagnetic minerals (e.g., lower χ_a, χ_{hf}, χ_{ferri}, ARM, and Fe content) but higher amount in high-coercivity phases (e.g., higher SIRM, MDF, and HIRM). The content of magnetite nanoparticles is drastically reduced than those in the marly units, as reflected by lower χ_{fd} (0.4%) and $\chi_{fd\text{-}normalized}$ (2.45%). Here, the goethite content is significantly lower, as shown by lower G% and RI ratio, while hematite dominates as the primary high-coercivity mineral (Figure 4b). This enrichment may be related to the circulation of hot coseismic fluids, relatively cold interseismic fluids, variations in peak temperature, or weathering (Liu et al., 2022; Tanaka et al., 2001; Yang et al., 2020; Zamani et al., 2023).

Finally, sandstones in the footwall contains lower concentrations of (titano-) magnetite and Fe-bearing clays, as shown by lower χ, χ_{hf}, ARM, Fe content, and χ_{ferri} (Figures 2 and 6, Figure S2 in Supporting Information S1). Grain size proxies and remanence loss values indicate a mixture of PSD to SD magnetite grains which are, on average, slightly coarser than those in the hanging wall, with no significant downward variations with distance (Figures S2 and S10 in Supporting Information S1). The footwall also contains a higher amount of hematite and/or goethite, as indicated by higher percentage of the B_{hard} components. This is evident at Gova, where MDF, B_{cr}, HIRM, and L-ratio values suggest an increase in high-coercivity minerals, likely controlled by lithology (Figure 2 and Figure S3 in Supporting Information S1). The occurrence of goethite in the footwall, in the first 3 m below the basal décollement, is documented by spaced FC-ZFC curves and increasing G% and R_{LT} (Figures 3 and 4, and Figure S10 in Supporting Information S1).

5.2. Comparison to Seismogenic Megathrusts Showing Coseismic Frictional Heating

In seismogenic megathrusts, the local occurrence of positive magnetic susceptibility anomalies in wall rocks has been associated with neoformation of ferrimagnetic phases induced by high-temperature (T > 400–500°C) frictional heating during past large earthquakes. Examples include the 1999 Chi-Chi earthquake (Mw 7.6) along the Chelungpu Fault (e.g., Chou et al., 2012; Mishima et al., 2009), the 2008 Wenchuan earthquake (Mw 7.9) along the Yingxiu-Beichuan and Anxian-Guanxian Faults (Cai et al., 2019; Liu et al., 2016; Yan et al., 2023), and the 2011 Tohoku-oki earthquake (Mw 9.0) along the Japan Trench plate boundary (Yang et al., 2018). In contrast, in other seismogenic zones such as the Nankai subduction megathrust, the Hikurangi margin, and locally along the Yingxiu-Beichuan fault, negative susceptibility anomalies and reduced M_s values, comparable to SVU, have been linked to a low slip rate (<1 m/s) and the absence of thermochemical alterations of Fe-bearing clays (e.g., Hirono et al., 2009; Yang et al., 2012b), anaerobic oxidation induced by methane-bearing fluids (Coffey et al., 2021; Greve et al., 2021) or to Fe^{2+} depletion from clay minerals and pyrite due to fluid circulation (Yang, Yang, et al., 2016). The latter could explain the decrease in χ_{hf} and χ_{ferri} values near the main slip surfaces in the marly units of the SVU.

In case of frictional heating, χ-T cycles are generally reversible up to ~400–500°C and show reduced neoformation of ferrimagnetic minerals (e.g., Yan et al., 2023; Yang, Dekkers, & Zhang, 2016). In contrast, our results (Figures 3c and 4c), with alteration starting at 350°C, resemble the χ-T cycles of fault gouges that have not been subjected to thermal events above 250–400°C (e.g., Tanikawa et al., 2008; Yan et al., 2023; Yang et al., 2012b), demonstrating the lack of thermal breakdown or decomposition of pyrite (T > 350–500°C; Bhargava et al., 2009; Yang et al., 2020) and/or Fe-bearing clays (T > 250–400°C; Hirono et al., 2009; Hirt et al., 1993; Tanikawa et al., 2008). Indeed, the increase in M_s and M_{rs} after thermal treatment from 250 to 350°C suggests the progressive neoformation of magnetite through termochemical reactions involving Fe^{3+} adsorbed on clay surfaces (e.g., smectite; Hirt et al., 1993), supporting reduced bulk specific heat and low coseismic temperatures (<250°C).

Hysteresis loops at RT trace those of gray gouge (characterized by mixed layers of illite/smectite) subjected to high-velocity friction (HVF) experiments at low slip rate (0.58–1.08 m/s) and T_{max} around 160–250°C, respectively (Yang et al., 2019). Only after thermal treatment at 450°C, SVU samples close to the major thrusts (Figure 5) reveal open loops and high B_c and M_{rs}/M_s values, resembling the illite-dominated gouge of the Yingxiu-Beichuan fault that experienced a T_{max} ~ 500°C (Yan et al., 2023). These data constrain the presence of a significant amount of goethite that altered into hematite during thermal treatment via progressive dehydration:

$$2\alpha FeOOH \iff \alpha Fe_2O_3 + H_2O \quad (1)$$

between 240 and 450°C (Dekkers, 1990; Till et al., 2015; Özdemir & Dunlop, 2000).

The occurrence of goethite in SVU samples is demonstrated by low-temperature experiments (e.g., spaced ZFC-FC curves and a high RI ratio; Figures 3 and 4). Goethite is common in fault gouges of seismogenic zones and has been linked to cooling of hot (T > 350°C) coseismic fluids and thermal pressurization processes (e.g., Chou et al., 2014; Mishima et al., 2006; Yan et al., 2023; Zamani et al., 2023; Zhang et al., 2017). However, it is rarely reported in fault gouge that did not experience temperatures >350°C, where its occurrence may instead be associated with fluid circulation or secondary alteration (Liu et al., 2014; Yang et al., 2012b).

Our low-temperature results show similarities with those of fault gouges that experienced temperatures <300–400°C (e.g., Mishima et al., 2009; Yang et al., 2012a, 2018) and slip-rate below 1.08 m/s (T_{peak} ~ 250°C; Yang et al., 2019). The suppressed P-transition, PM_{ZFC}, and RT-SIRM values, resemble the characteristics of claystones subjected to T_{max} between 60 and 350°C (Abdelmalak & Polteau, 2020; Aubourg et al., 2019; Aubourg & Pozzi, 2010; Blaise et al., 2014), confirming a relatively low temperature for the SVU.

In the SVU, the absence of pyrrhotite (e.g., lack of Besnus transition; Figures 3 and 4) excludes coseismic pyrite decomposition at T > 500°C (e.g., Chen et al., 2019; Uchida et al., 2024; Yang et al., 2018) and diagenetic pyrrhotite formation between 250 and 350°C (Aubourg et al., 2019; Roberts, 2015), supporting T < 250°C. However, the lack of high-temperature evidence in the studied transects does not completely rule out the occurrence of frictional heating at other localities or depths, as observed in the Yingxiu-Beichuan and Anxian-

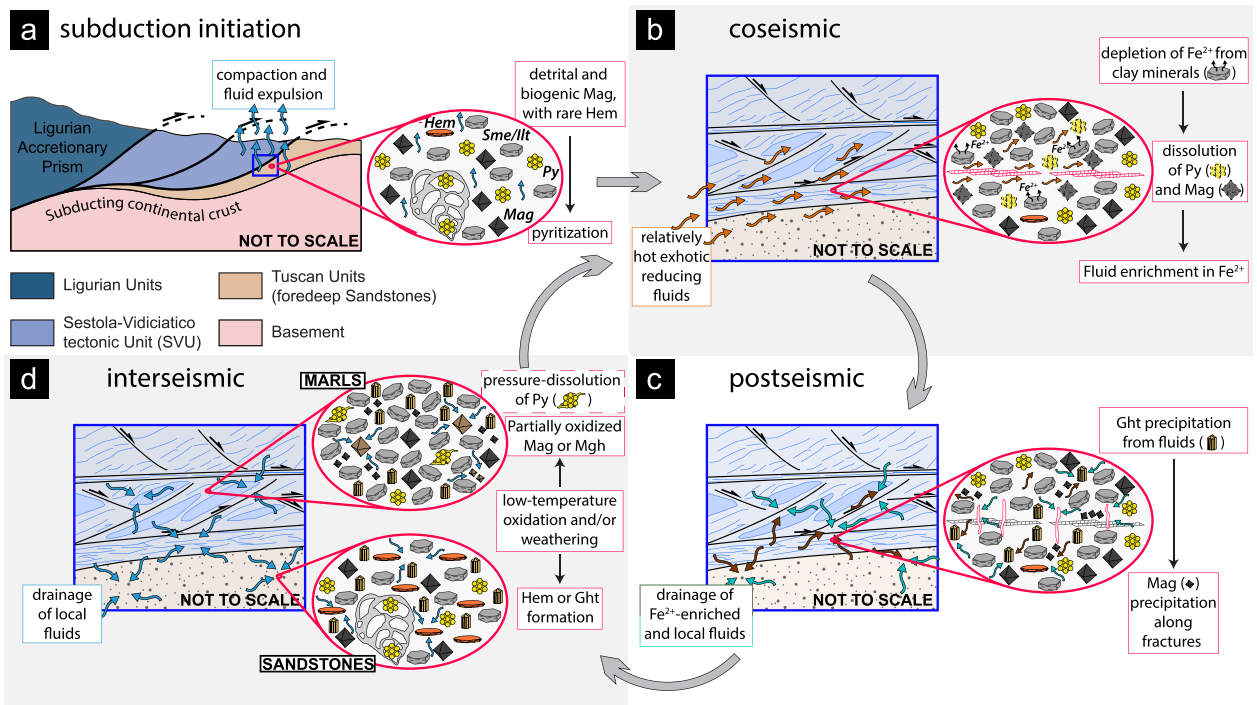

Figure 7. Schematic summary of fluid circulation pathways and changes in magnetic minerals across the SVU megathrust due to fluid-rock interaction during the seismic cycle: (a) subduction initiation with sedimentary and diagenetic features; (b) coseismic dissolution and deplation processes; (c) postseismic precipitation of Fe-bearing minerals; (d) interseismic oxidation and/or weathering.

Guanxian Faults, where records of both temperature <250–400°C (Liu et al., 2014; Yang et al., 2012a, Yang et al., 2012b) and >500°C with pyrrhotite formation have been reported (Yan et al., 2023).

The absence of direct evidence for greigite, coupled with relatively low SIRM/χ_{ferri} (~5 kA/m), M_{rs}/M_s values and relatively high remanence loss, suggest near-complete pyritization during burial or due to advection of methane-bearing fluids (Kars et al., 2021; Musgrave et al., 2019; Schoonen, 2004).

Pyrite is frequently reported in the fault gouge of seismogenic zones in the form of small isolated framboids or chains along fractures and deformation bands (e.g., Chen et al., 2016; Chou et al., 2012; Fabbri et al., 2020; Famin et al., 2021). In cases of high temperature coseismic frictional heating, either a pyrrhotite core or rim has been observed around or within pyrite grains (Chou et al., 2012; Yan et al., 2023). In contrast, in the SVU, large (~150 μm) aggregates of framboidal pyrite, primarily in the sandstones, are associated with preserved bioclasts (Figure 6d), suggesting a diagenetic origin. Moreover, in marly units, the presence of isolated framboids (1–10 μm) and shadow-like pyrite tails (Figure 6a) along deformation bands reveals significant structural control in their formation but no evidence of thermal alteration are observed.

5.3. Implications for Fluid-Rock Interaction During the Seismic Cycle

The variations in rock magnetic properties of the wall rocks across the shallower portions of the SVU demonstrate relatively low maximum bulk heating ($T < 250$°C) during the seismic cycle, with a limited influence of frictional heating on the alterations of Fe-bearing minerals. Instead, the results reveal a history of active fluid circulation and changes in fluid redox conditions, which can be correlated with fluctuation in fluid pressure.

During the early phases of subduction, the sediments involved in the SVU were fluid-rich and not completely lithified (Mittempergher et al., 2018; Vannucchi et al., 2010). Seawater may have been the primary fluid source, resulting in relatively oxidizing conditions (Fabbri et al., 2020; Yamaguchi et al., 2011). In this context, (titano-) magnetites are reported as the main Fe-bearing oxides, with hematite being minor or absent (e.g., Li et al., 2015; Shi et al., 2017; Zhao et al., 2013; Figure 7a). Similar magnetic mineralogy has been observed in syn-orogenic foredeep turbidites from the Northern Appenines not involved within the SVU (e.g., Caricchi et al., 2016).

The local association of framboidal pyrite with undeformed bioclasts (particularly in sandstones, Figure 6d), the sparse presence of pyrite within silicate sheets and the occurrence of greigite (even if significantly limited) suggest that sediments involved within the SVU may have experienced earlier sulfate reduction to some extent with relatively limited reductive dissolution, as biogenic and detrital magnetites appear to be partially preserved. In addition, the enrichment in pyrite along deformed domain (especially in marly units, Figure S14 in Supporting Information S1) is interpreted as a late diagenetic near-complete pyritization potentially occurred during embedding in the megathrust and favored by local circulation of methane-bearing fluids (e.g., Conti et al., 2021).

In this framework, the observed variation in (titano-)magnetite concentration and grain size between marls and sandstones is believed to reflect a primary lithological feature (i.e., different detrital and biogenic magnetite content).

As subduction progresses, sediments undergo compaction, porosity reduction, and fluid expulsion, resulting to near-lithostatic overpressure along intraplate shear zones, leading to seismic failure (e.g., Screaton & Saffer, 2005; Sibson, 2013).

During the coseismic phase, failure and re-shearing along major faults result in a significant increase in fault-parallel permeability and a drop in fluid pressure (Mitchell & Faulkner, 2012; Sibson, 2013). Likely relatively hot exhotic fluids, potentially from dehydration reactions at depth (Vannucchi et al., 2010), pervade fault zones, promoting fluid-rock interaction and depletion processes (Chen et al., 2013; Hashimoto & Kaji, 2012; Yang, Yang, et al., 2016; Figure 7b). The general decrease in iron-oxides and Fe-bearing paramagnetic minerals close to the main thrust suggest localized processes related to the circulation of fluids in disequilibrium with the wall rocks.

Selective breakdown/alteration of pyrite and depletion of Fe^{2+} from clays in the wall rock near the main thrusts is inferred from lower χ_{hf} values, SEM-EDS and multispectral image analysis and alteration indices (Figures S1 and S14, and Table S7 in Supporting Information S1). Additionally, the generally low concentration in magnetite and its overall decrease close to the basal thrusts suggests pervasive to partial corrosion/dissolution of detrital and biogenic magnetite through reductive chemical alteration (Cornell & Schwertmann, 2003; Otake et al., 2010):

$$1/3Fe_3O_4 + 2H^+ + 1/3H_2 \iff Fe^{2+} + 4/3H_2O \quad (2)$$

potentially enhanced by dissolved sufildes (Poulton et al., 2004):

$$Fe_3O_4 + H_2S + 6H^+ \iff 3Fe^{2+} + S^\circ + 4H_2O \quad (3)$$

To occur, magnetite dissolution requires reducing conditions (suggested by positive Eu^{2+} anomaly of the shear veins; Cerchiari et al., 2020) and relatively low pH (potentially favored by local pyrite dissolution; Chou et al., 2012) to maintain Fe^{2+} as acqueous phase (Cornell & Schwertmann, 2003; Poulton et al., 2004). These processes collectively lead to fluid enrichment in Fe^{2+} during the coseismic phase.

In the immediate postseimic phase, (calcite) veins precipitation reduces slip surfaces permeability, inducing fluids to flows in adjacent fractured zones (Kimura et al., 1997, 2014; Morris et al., 2003; Screaton & Saffer, 2005). Local variation in differential stress and pore pressure promotes the switching of stress regime to extentional, so that fault-perpendicular fractures and veinlets form in equilibrium with the local fluids (see Cerchiari et al., 2020 for details).

In this framework, the relative enrichments in goethite and SD magnetite with distance (Figures 2 and 4a), may suggests rapid migration/escape of Fe^{2+}-enriched fluids, with precipitation promoted by interaction with less reducing (likely neutral to slightly alkaline) local fluids (Cerchiari et al., 2020; Yamaguchi et al., 2011; Figure 7c). These conditions allow the oxidation of Fe^{2+} and the precipitation of iron-hydroxides at relatively low (<200°C) temperatures (Cornell & Schwertmann, 2003):

$$2Fe^{2+} + 3H_2O + 1/2O_2 \iff 2FeOOH + 4H^+ \quad (4)$$

Additionally, a possible local circulation of CO_2-bearing fluids may promote direct precipitation of goethite over hematite from Fe^{2+}-rich solutions (Cornell & Schwertmann, 2003):

$$4Fe^{2+} + O_2 + 4CaCO_3 + 2H_2O \iff 4FeOOH + 4Ca^{2+} + 4CO_2 \quad (5)$$

The latter sourse can possibly be ascribed to decarbonation processes (Zamani et al., 2023) at depth or a combination of pressure solution and local sorption and complexation reactions (Cerchiari et al., 2020).

Correlation between neoformed SD magnetite with overpressure and upward migration of Fe^{2+}-enriched fluids in extensional regimes is corroborated by the magnetic fabric analysis of Robustelli Test and Zanella (2021). Moreover, local enrichment of goethite and SP magnetite nanoparticles near major thrusts, may aligns with inclusion of Fe-oxides within syntectonic veins (Vannucchi et al., 2010). In addition, the absence of evidence of high-temperature frictional heating supports the formation of SP grains via precipitation from a Fe^{2+} enriched fluids during the post seismic phase (Chou et al., 2014; Ma et al., 2006).

Finally, during the interseismic phase, fluids are in equilibrium with the wall rocks, mantaining a relativily oxidizing conditions and neutral to slightly alkaline pH, a compressional regime is recovered, and fluid pressure increases (Cerchiari et al., 2020; Yamaguchi et al., 2011). Especially in marly units, compaction induces pressure-solution of pyrite leading to the formation of dispersed micro-framboids along dissolution seams (Figure 6a).

Under these conditions, magnetic minerals may be subjected to some degree of alteration and/or weathering (Liu et al., 2022; Tanaka et al., 2001; Figure 7d). For instance, the occurrence of hematite within sandstones may result from the oxidation of magnetite due to low-temperature alteration or surface wheathering:

$$4Fe_3O_4 + O_2 \iff 6Fe_2O_3 \quad (6)$$

Hematite formation from magnetite might also be related to local circulation of CO_2-bearing fluids (Liu et al., 2022):

$$2Fe_3O_4 + CO_2 \iff 3Fe_2O_3 + CO \quad (7)$$

The absence of hematite in the marls could be attributed to reduced avalability of oxigen due to their low permeability. In contrast, low-temperature oxidation may explain the local presence of partially oxidized magnetite/maghemite in marls.

Magnetic mineralogy and related concentrations can be modified during subsequent seismic cycles and exhumation, potentially leading to heterogeneities among different outcrops. For example, goethite can form under oxidizing conditions, for the introduction of meteoric water during exhumation phases (Evans et al., 1997; Tanaka et al., 2001). This process might partially explain the occurrence of goethite in sandstones, potentially formed as an early transitional phase in the alteration of ferrihydrite to hematite (Bilardello et al., 2020; Jiang et al., 2018). Variations in goethite grain size between transects might reflect slightly different redox-conditions and fluid temperatures during subsequent seismic events. For example, the higher content of nano-goethite at Gova, may suggest precipitation from a relatively colder and neutral fluids (Cornell & Schwertmann, 2003). In contrast, the higher concentration of coarser-grained goethite, together with an apparently higher Al-substitution, at Site T1-B3 (at higher distance) might suggest the circulation of slightly hotter and more alkaline fluids along different surfaces during repeated seismic cycles and/or relvant interaction with the clay-rich wall rocks (Cornell & Schwertmann, 2003) during longer interseismic periods, favoring oxidation and weathering. Lastly, the localization of significant amounts of hematite in the sheared sandstones may result from the dehydration of goethite (Equation 1) via interaction with relatively hot exhotic fluids during cyclical seismic events (reasonably at T ~200–300°C; Zamani et al., 2023).

6. Conclusions

We investigated the magnetic properties of fault rocks from an exhumed megathrust shear zone, where no evidence of frictional heating has been recorded, to identify fluid-induced changes in magnetic mineral assemblages, concentrations, and grain size induced during seismic cycles. Our results reveal partial preservation of sedimentary and diagenetic features, including undeformed framboidal pyrites and lithologically related variations in magnetite grain size and concentration. Low concentrations of ferrimagnetic minerals, along with reduced χ_{hf}, Fe content and alteration indices near the main thrusts, suggest Fe^{2+} depletion from clays and the partial dissolution

of pyrite and magnetite, driven by the circulation of exhotic coseismic fluids. In contrast, increasing magnetite and goethite concentration with distance, particularly in the more porous sandstones of the lower plate, indicate Fe^{2+}-enriched fluid migration and interaction with local fluids during the postseismic phase. Hematite in sandstones and partially oxidized magnetite/maghemite in marls reflect oxidation during prolonged interseismic phases. Heterogeneities in mineral assemblages and concentrations among localities further support cyclic fluid circulation linked with successive seismic events.

This study highlights the potential of detailed magnetic analyses to trace fluid circulation during seismic cycles. However, given the observed heterogeneities between outcrops along the same megathrust shear zone, further research on both active and exhumed megathrusts with relatively mild temperatures is needed to corroborate these interpretations and assess their broader significance.

Data Availability Statement

Rock magnetic data are reported in Supporting Information and available at Zenodo (Robustelli Test et al., 2025) with a Creative Commons Attribution 4.0 International.

Acknowledgments
We thank Ramon Egli, Eric Ferré and an anonymous reviewer for their thorough and constructive reviews, which have helped us to significantly improve this manuscript. This project was funded by MIUR ex-60% attributed to EZ and PhD grants-Budget 10% attributed to CRT. Field work was supported by MIUR ex-60% and MIUR research Grants Cofin-PRIN 2020 "POEM project–POligEnetic Melanges: anatomy, significance and societal impact", Grants 2020542ET7_003 attributed to AF. CRT acknowledges the Visiting Fellowship at the Institute for Rock Magnetism (IRM). The IRM is a US National Multi-user Facility supported through the Instrumentation and Facilities program of the National Science Foundation, Earth Sciences Division (NSF-EAR 2153786), and funding from the University of Minnesota. Max Brown, Joshua Feinberg, Bruce Moskowitz and Peat Solheid are thanked for helpful discussions and advice during CRT's Visiting Fellowship. Open access publishing facilitated by Universita degli Studi di Torino, as part of the Wiley - CRUI-CARE agreement.

References

Abdelmalak, M. M., & Polteau, S. (2020). The thermal maturity of sedimentary basins as revealed by magnetic mineralogy. *Basin Research*, *32*(6), 1510–1531. https://doi.org/10.1111/bre.12439

Aubourg, C., Jackson, M., Ducoux, M., & Mansour, M. (2019). Magnetite-out and pyrrhotite-in temperatures in shales and slates. *Terra Nova*, *31*(6), 534–539. https://doi.org/10.1111/ter.12424

Aubourg, C., Kars, M., Pozzi, J.-P., Mazurek, M., & Grauby, O. (2021). A magnetic geothermometer in moderately buried shales. *Minerals*, *11*(9), 957. https://doi.org/10.3390/min11090957

Aubourg, C., & Pozzi, J.-P. (2010). Toward a new <250°C pyrrhotite–magnetite geothermometer for claystones. *Earth and Planetary Science Letters*, *294*(1–2), 47–57. https://doi.org/10.1016/j.epsl.2010.02.045

Bhargava, S. K., Garg, A., & Subasinghe, N. D. (2009). In situ high-temperature phase transformation studies on pyrite. *Fuel*, *88*(6), 988–993. https://doi.org/10.1016/j.fuel.2008.12.005

Bilardello, D. (2025). Rock-Paleo-Magnetism: Tools for processing magnetic data in paleomagnetism and rock magnetism. *GitHub*. https://github.com/yourusername/Rock-Paleo-Magnetism

Bilardello, D., Banerjee, S. K., Volk, M. W. R., Soltis, J. A., & Penn, R. L. (2020). Simulation of natural iron oxide alteration in soil: Conversion of synthetic ferrihydrite to hematite without Artificial dopants, observed with magnetic methods. *Geochemistry, Geophysics, Geosystems*, *21*(7), e2020GC009037. https://doi.org/10.1029/2020GC009037

Blaise, T., Barbarand, J., Kars, M., Ploquin, F., Aubourg, C., Brigaud, B., et al. (2014). Reconstruction of low temperature (<100°C) burial in sedimentary basins: A comparison of geothermometer in the intracontinental Paris basin. *Marine and Petroleum Geology*, *53*, 71–87. https://doi.org/10.1016/j.marpetgeo.2013.08.019

Botti, F., Aldega, L., & Corrado, S. (2004). Sedimentary and tectonic burial evolution of the northern Apennines in the Modena-Bologna area: Constraints from combined stratigraphic, structural, organic matter and clay mineral data of Neogene thrust-top basins. *Geodinamica Acta*, *17*(3), 185–203. https://doi.org/10.3166/ga.17.185-203

Botti, F., Daniele, G., Baldacci, F., Palandri, S., Ribolini, A., Ungari, A., & Molli, G. (2011). *Note illustrative Della Carta Geologica d'Italia Alla Scala 1:50.000, Foglio 251 "Porretta Terme"*. Servizio Geologico d'Italia. Retrieved from https://www.isprambiente.gov.it/Media/carg/note_illustrative/251_Porretta_Terme.pdf

Cai, Y., Pei, J., Wang, H., Sheng, M., & Si, J. (2019). Paleo-earthquakes revealed by rock magnetic evidence from the Anxian-Guanxian fault, Sichuan Province, China. *Tectonophysics*, *752*, 68–80. https://doi.org/10.1016/j.tecto.2018.12.027

Caricchi, C., Cifelli, F., Kissel, C., Sagnotti, L., & Mattei, M. (2016). Distinct magnetic fabric in weakly deformed sediments from extensional basins and fold-and-thrust structures in the northern Apennine orogenic belt (Italy): AMS analysis of weakly deformed deposits. *Tectonics*, *35*(2), 238–256. https://doi.org/10.1002/2015TC003940

Carlini, M., Artoni, A., Aldega, L., Balestrieri, M. L., Corrado, S., Vescovi, P., et al. (2013). Exhumation and reshaping of far-travelled/allochthonous tectonic units in mountain belts. New insights for the relationships between shortening and coeval extension in the western Northern Apennines (Italy). *Tectonophysics*, *608*, 267–287. https://doi.org/10.1016/j.tecto.2013.09.029

Carter-Stiglitz, B., Moskowitz, B., & Jackson, M. (2004). More on the low-temperature magnetism of stable single domain magnetite: Reversibility and non-stoichiometry. *Geophysical Research Letters*, *31*(6), 2003GL019155. https://doi.org/10.1029/2003GL019155

Cerchiari, A., Remitti, F., Mittempergher, S., Festa, A., Lugli, F., & Cipriani, A. (2020). Cyclical variations of fluid sources and stress state in a shallow megathrust-zone mélange. *Journal of the Geological Society*, *177*(3), 647–659. https://doi.org/10.1144/jgs2019-072

Chang, L., Winklhofer, M., Roberts, A. P., Heslop, D., Florindo, F., Dekkers, M. J., et al. (2013). Low-temperature magnetic properties of pelagic carbonates: Oxidation of biogenic magnetite and identification of magnetosome chains: Magnetism of pelagic carbonates. *Journal of Geophysical Research: Solid Earth*, *118*(12), 6049–6065. https://doi.org/10.1002/2013JB010381

Charpentier, D., Milesi, G., Labaume, P., Abd Elmola, A., Buatier, M., Lanari, P., & Muñoz, M. (2024). Evolution of fluid redox in a fault zone of the Pic de Port-Vieux thrust in the Pyrenees Axial Zone (Spain). https://doi.org/10.5194/egusphere-2024-386

Chen, J., Yang, X., Ma, S., & Spiers, C. J. (2013). Mass removal and clay mineral dehydration/rehydration in carbonate-rich surface exposures of the 2008 Wenchuan Earthquake fault: Geochemical evidence and implications for fault zone evolution and coseismic slip. *Journal of Geophysical Research: Solid Earth*, *118*(2), 474–496. https://doi.org/10.1002/jgrb.50089

Chen, J., Yang, X., Ma, S., Yang, T., & Niemeijer, A. (2016). Hydraulic properties of samples retrieved from the Wenchuan earthquake Fault Scientific Drilling Project Hole-1 (WFSD-1) and the surface rupture zone: Implications for coseismic slip weakening and fault healing. *Geochemistry, Geophysics, Geosystems*, *17*(7), 2717–2744. https://doi.org/10.1002/2016GC006376

Chen, Y.-H., Chen, Y.-H., Hsu, W.-D., Chang, Y.-C., Sheu, H.-S., Lee, J.-J., & Lin, S.-K. (2019). Using the high-temperature phase transition of iron sulfide minerals as an indicator of fault slip temperature. *Scientific Reports*, *9*(1), 7950. https://doi.org/10.1038/s41598-019-44319-8

Chou, Y., Song, S., Aubourg, C., Lee, T., Song, Y., & Yeh, E. (2014). Quantitative modeling of the newly formed magnetic minerals in the fault gouge of 1999 Chi-Chi earthquake (M_w 7.6), Taiwan. *Journal of Geophysical Research: Solid Earth*, *119*(9), 6771–6781. https://doi.org/10.1002/2014JB011098

Chou, Y.-M., Song, S.-R., Aubourg, C., Song, Y.-F., Boullier, A.-M., Lee, T.-Q., et al. (2012). Pyrite alteration and neoformed magnetic minerals in the fault zone of the Chi-Chi earthquake (M_w 7.6, 1999): Evidence for frictional heating and co-seismic fluids: Pyrite alteration in the fault zone. *Geochemistry, Geophysics, Geosystems*, *13*(8). https://doi.org/10.1029/2012GC004120

Coffey, G. L., Savage, H. M., Polissar, P. J., Meneghini, F., Ikari, M. J., Fagereng, Å., et al. (2021). Evidence of seismic slip on a large Splay fault in the Hikurangi subduction zone. *Geochemistry, Geophysics, Geosystems*, *22*(8), e2021GC009638. https://doi.org/10.1029/2021GC009638

Conti, S., Argentino, C., Fioroni, C., Salocchi, A. C., & Fontana, D. (2021). Miocene seep-carbonates of the northern Apennines (Emilia to Umbria, Italy): An overview. *Geosciences*, *11*(2), 53. https://doi.org/10.3390/geosciences11020053

Cornamusini, G. C., Conti, P. C., & Bambini, A. M. B. (2018). The late Oligocene to early Miocene foredeep basin system evolution of the Northern Apennines (Emilia-Tuscany, Italy): Review and new Litho-biostratigraphic data. *Italian Journal of Geosciences*, *137*(3), 396–419. https://doi.org/10.3301/IJG.2018.06

Cornell, R. M., & Schwertmann, U. (2003). *The Iron oxides: Structure, properties, reactions, occurences and uses* (1st ed.). Wiley. https://doi.org/10.1002/3527602097

Day, R., Fuller, M., & Schmidt, V. A. (1977). Hysteresis properties of titanomagnetites: Grain-size and compositional dependence. *Physics of the Earth and Planetary Interiors*, *13*(4), 260–267. https://doi.org/10.1016/0031-9201(77)90108-X

Dearing, J. A., Dann, R. J. L., Hay, K., Lees, J. A., Loveland, P. J., Maher, B. A., & O'Grady, K. (1996). Frequency-dependent susceptibility measurements of environmental materials. *Geophysical Journal International*, *124*(1), 228–240. https://doi.org/10.1111/j.1365-246X.1996.tb06366.x

Dekkers, M. J. (1989). Magnetic properties of natural goethite-Ii. TRM behaviour during thermal and alternating field demagnetization and low-temperature treatment. *Geophysical Journal International*, *97*(2), 341–355. https://doi.org/10.1111/j.1365-246X.1989.tb00505.x

Dekkers, M. J. (1990). Magnetic properties of natural goethite-III. Magnetic behaviour and properties of minerals originating from goethite dehydration during thermal demagnetization. *Geophysical Journal International*, *103*(1), 233–250. https://doi.org/10.1111/j.1365-246X.1990.tb01765.x

Dunlop, D. J. (2002a). Theory and application of the Day plot (M_{rs}/M_s versus H_{cr}/H_c) 1. Theoretical curves and tests using titanomagnetite data. *Journal of Geophysical Research*, *107*(B3). https://doi.org/10.1029/2001JB000486

Dunlop, D. J. (2002b). Theory and application of the Day plot (M_{rs}/M_s versus H_{cr}/H_c) 2. Application to data for rocks, sediments, and soils. *Journal of Geophysical Research*, *107*(B3), 2057. https://doi.org/10.1029/2001JB000487

Dunlop, D. J., & Argyle, K. S. (1991). Separating multidomain and single-domain-like remanences in pseudo-single-domain magnetites (215–540 nm) by low-temperature demagnetization. *Journal of Geophysical Research*, *96*(B2), 2007–2017. https://doi.org/10.1029/90JB02338

Egli, R. (2004a). Characterization of individual rock magnetic components by analysis of remanence curves, 1. Unmixing natural sediments. *Studia Geophysica et Geodaetica*, *48*(2), 391–446. https://doi.org/10.1023/B:SGEG.0000020839.45304.6d

Egli, R. (2013). VARIFORC: An optimized protocol for calculating non-regular First-Order Reversal Curve (FORC) diagrams. *Global and Planetary Change*, *110*, 302–320. https://doi.org/10.1016/j.gloplacha.2013.08.003

Egli, R. (2021). Magnetic characterization of geologic materials with first-order reversal curves. In V. Franco & B. Dodrill (Eds.), *Magnetic measurement techniques for materials characterization* (pp. 455–604). Springer International Publishing. https://doi.org/10.1007/978-3-030-70443-8_17

Egli, R. (2023). VARIFORC v. 5.0 (5.0). *Zenodo*, *110*, 302–320. https://doi.org/10.1016/j.gloplacha.2013.08.003

Egli, R., & Lowrie, W. (2002). Anhysteretic remanent magnetization of fine magnetic particles. *Journal of Geophysical Research*, *107*(B10). https://doi.org/10.1029/2001jb000671

Evans, J. P., Forster, C. B., & Goddard, J. V. (1997). Permeability of fault-related rocks, and implications for hydraulic structure of fault zones. *Journal of Structural Geology*, *19*(11), 1393–1404. https://doi.org/10.1016/S0191-8141(97)00057-6

Fabbri, O., Goldsby, D. L., Chester, F., Karpoff, A. M., Morvan, G., Ujiie, K., et al. (2020). Deformation structures from splay and décollement faults in the Nankai accretionary prism, SW Japan (IODP NanTroSEIZE expedition 316): Evidence for slow and rapid slip in fault rocks. *Geochemistry, Geophysics, Geosystems*, *21*(6), e2019GC008786. https://doi.org/10.1029/2019GC008786

Famin, V., Raimbourg, H., Andreani, M., & Boullier, A.-M. (2021). Deformation-enhanced diagenesis and bacterial proliferation in the Nankai accretionary prism. *Solid Earth*, *12*(9), 2067–2085. https://doi.org/10.5194/se-12-2067-2021

Fulton, P. M., & Brodsky, E. E. (2016). In situ observations of earthquake-driven fluid pulses within the Japan trench plate boundary fault zone. *Geology*, *44*(10), 851–854. https://doi.org/10.1130/G38034.1

Greve, A., Kars, M., & Dekkers, M. J. (2021). Fluid accumulation, migration and anaerobic oxidation of methane along a major splay fault at the Hikurangi subduction margin (New Zealand): A magnetic approach. *Journal of Geophysical Research: Solid Earth*, *126*(2), e2020JB020671. https://doi.org/10.1029/2020JB020671

Guyodo, Y., Mostrom, A., Lee Penn, R., & Banerjee, S. K. (2003). From Nanodots to Nanorods: Oriented aggregation and magnetic evolution of nanocrystalline goethite. *Geophysical Research Letters*, *30*(10), 2003GL017021. https://doi.org/10.1029/2003GL017021

Hashimoto, Y., & Kaji, U. (2012). Rock-fluid interaction along seismogenic faults infered from clay minerals in Okitsu mélange, the cretaceous Shimanto belt, SW Japan. In S. DAmico (Ed.), *Earthquake research and analysis—seismology, seismotectonic and earthquake geology*. InTech. https://doi.org/10.5772/29951

Heslop, D., Dekkers, M. J., Kruiver, P. P., & Van Oorschot, I. H. M. (2002). Analysis of isothermal remanent magnetization acquisition curves using the expectation-maximization algorithm. *Geophysical Journal International*, *148*(1), 58–64. https://doi.org/10.1046/j.0956-540x.2001.01558.x

Hirono, T., Ikehara, M., Otsuki, K., Mishima, T., Sakaguchi, M., Soh, W., et al. (2006). Evidence of frictional melting from disk-shaped black material, discovered within the Taiwan Chelungpu fault system. *Geophysical Research Letters*, *33*(19), 2006GL027329. https://doi.org/10.1029/2006GL027329

Hirono, T., Ujiie, K., Ishikawa, T., Mishima, T., Hamada, Y., Tanimizu, M., et al. (2009). Estimation of temperature rise in a shallow slip zone of the megasplay fault in the Nankai Trough. *Tectonophysics*, *478*(3–4), 215–220. https://doi.org/10.1016/j.tecto.2009.08.001

Hirt, A. M., Banin, A., & Gehring, A. U. (1993). Thermal generation of ferromagnetic minerals from iron-enriched smectites. *Geophysical Journal International*, *115*(3), 1161–1168. https://doi.org/10.1111/j.1365-246X.1993.tb01518.x

Housen, B. A., & Moskowitz, B. M. (2006). Depth distribution of magnetofossils in near-surface sediments from the Blake/Bahama Outer Ridge, western North Atlantic Ocean, determined by low-temperature magnetism. *Journal of Geophysical Research*, *111*(G1), 2005JG000068. https://doi.org/10.1029/2005JG000068

Housen, B. A., & Musgrave, R. J. (1996). Rock-magnetic signature of gas hydrates in accretionary prism sediments. *Earth and Planetary Science Letters*, *139*(3–4), 509–519. https://doi.org/10.1016/0012-821X(95)00245-8

Hrouda, F., Chlupáčová, M., & Mrázová, Š. (2006). Low-field variation of magnetic susceptibility as a tool for magnetic mineralogy of rocks. *Physics of the Earth and Planetary Interiors*, *154*(3–4), 323–336. https://doi.org/10.1016/j.pepi.2005.09.013

Hrouda, F., Müller, P., & Hanák, J. (2003). Repeated progressive heating in susceptibility vs. Temperature investigation: A new palaeotemperature indicator? *Physics and Chemistry of the Earth, Parts A/B/C*, *28*(16–19), 653–657. https://doi.org/10.1016/S1474-7065(03)00119-0

Jackson, M., Borradaile, G., Hudleston, P., & Banerjee, S. (1993). Experimental deformation of synthetic magnetite-bearing calcite sandstones: Effects on remanence, bulk magnetic properties, and magnetic anisotropy. *Journal of Geophysical Research*, *98*(B1), 383–401. https://doi.org/10.1029/92jb01028

Jackson, M., Bowles, J. A., & Banerjee, S. K. (2011). Interpretation of low- temperature data Part V: The magnetite Verwey transition (Part B): Field-cooling effects on stoichiometric magnetite below TV. *The IRM Quarterly*, *21*(4).

Jackson, M., Moskowitz, B., Rosenbaum, J., & Kissel, C. (1998). Field-dependence of AC susceptibility in titanomagnetites. *Earth and Planetary Science Letters*, *157*(3–4), 129–139. https://doi.org/10.1016/S0012-821X(98)00032-6

Jackson, M., & Solheid, P. (2010). On the quantitative analysis and evaluation of magnetic hysteresis data: Hysteresis loop evaluation and analysis. *Geochemistry, Geophysics, Geosystems*, *11*(4). https://doi.org/10.1029/2009GC002932

Jiang, Z., Liu, Q., Roberts, A. P., Barrón, V., Torrent, J., & Zhang, Q. (2018). A new model for transformation of ferrihydrite to hematite in soils and sediments. *Geology*. https://doi.org/10.1130/G45386.1

Kars, M., Greve, A., & Zerbst, L. (2021). Authigenic greigite as an indicator of methane diffusion in gas hydrate-bearing sediments of the Hikurangi margin, New Zealand. *Frontiers in Earth Science*, *9*, 603363. https://doi.org/10.3389/feart.2021.603363

Kars, M., Lerouge, C., Grangeon, S., Aubourg, C., Tournassat, C., Madé, B., & Claret, F. (2015). Identification of nanocrystalline goethite in reduced clay formations: Application to the Callovian-Oxfordian formation of Bure (France). *American Mineralogist*, *100*(7), 1544–1553. https://doi.org/10.2138/am-2015-5096

Kimura, G., Silver, E., Blum, P., Blanc, G., Bolton, A., Clennell, M. B., et al. (1997). *Proceedings of the ocean drilling program, 170 initial reports* (Vol. 170). Ocean Drilling Program. https://doi.org/10.2973/odp.proc.ir.170.1997

Kimura, S., Kaneko, H., Ito, T., & Minagawa, H. (2014). The effect of effective normal stress on particle breakage, porosity and permeability of sand: Evaluation of faults around methane hydrate reservoirs. *Tectonophysics*, *630*, 285–299. https://doi.org/10.1016/j.tecto.2014.05.031

King, J. W., & Channell, J. E. T. (1991). Sedimentary magnetism, environmental magnetism, and magnetostratigraphy. *Reviews of Geophysics*, *29*(S1), 358–370. https://doi.org/10.1002/rog.1991.29.s1.358

Kruiver, P. P., Dekkers, M. J., & Heslop, D. (2001). Quantification of magnetic coercivity components by the analysis of acquisition curves of isothermal remanent magnetisation. *Earth and Planetary Science Letters*, *189*(3–4), 269–276. https://doi.org/10.1016/S0012-821X(01)00367-3

Li, Y., Zhao, X., Jovane, L., Petronotis, K. E., Gong, Z., & Xie, S. (2015). Paleomagnetic constraints on the tectonic evolution of the Costa Rican subduction zone: New results from sedimentary successions of IODP drill sites from the Cocos Ridge. *Geochemistry, Geophysics, Geosystems*, *16*(12), 4479–4493. https://doi.org/10.1002/2015GC006058

Liu, D., Ferré, E. C., Li, H., Chou, Y.-M., Wang, H., Horng, C.-S., et al. (2022). Magnetic evidence of seismic fluid processes along the East Yibug Chaka fault, Tibet. *Tectonophysics*, *838*, 229500. https://doi.org/10.1016/j.tecto.2022.229500

Liu, D., Li, H., Lee, T.-Q., Chou, Y.-M., Song, S.-R., Sun, Z., et al. (2014). Primary rock magnetism for the Wenchuan earthquake fault zone at Jiulong outcrop, Sichuan Province, China. *Tectonophysics*, *619–620*, 58–69. https://doi.org/10.1016/j.tecto.2013.08.028

Liu, D., Li, H., Lee, T.-Q., Sun, Z., Liu, J., Han, L., & Chevalier, M.-L. (2016). Magnetic mineral characterization close to the Yingxiu-Beichuan fault surface rupture zone of the Wenchuan earthquake (Mw 7.9, 2008) and its implication for earthquake slip processes. *Journal of Asian Earth Sciences*, *115*, 468–479. https://doi.org/10.1016/j.jseaes.2015.10.019

Liu, P., Hirt, A. M., Schüler, D., Uebe, R., Zhu, P., Liu, T., & Zhang, H. (2019). Numerical unmixing of weakly and strongly magnetic minerals: Examples with synthetic mixtures of magnetite and hematite. *Geophysical Journal International*, *217*(1), 280–287. https://doi.org/10.1093/gji/ggz022

Liu, Q., Roberts, A. P., Torrent, J., Horng, C., & Larrasoaña, J. C. (2007). What do the HIRM and *S* -ratio really measure in environmental magnetism? *Geochemistry, Geophysics, Geosystems*, *8*(9), 2007GC001717. https://doi.org/10.1029/2007GC001717

Liu, Q., Yu, Y., Torrent, J., Roberts, A. P., Pan, Y., & Zhu, R. (2006). Characteristic low-temperature magnetic properties of aluminous goethite [α -(Fe, Al)OOH] explained. *Journal of Geophysical Research*, *111*(B12), 2006JB004560. https://doi.org/10.1029/2006JB004560

Ma, K.-F., Tanaka, H., Song, S.-R., Wang, C.-Y., Hung, J.-H., Tsai, Y.-B., et al. (2006). Slip zone and energetics of a large earthquake from the Taiwan Chelungpu-fault Drilling project. *Nature*, *444*(7118), 473–476. https://doi.org/10.1038/nature05253

Maher, B. A. (1988). Magnetic properties of some synthetic sub-micron magnetites. *Geophysical Journal International*, *94*(1), 83–96. https://doi.org/10.1111/j.1365-246X.1988.tb03429.x

Maxbauer, D. P., Feinberg, J. M., & Fox, D. L. (2016a). Magnetic mineral assemblages in soils and paleosols as the basis for paleoprecipitation proxies: A review of magnetic methods and challenges. *Earth-Science Reviews*, *155*, 28–48. https://doi.org/10.1016/j.earscirev.2016.01.014

Maxbauer, D. P., Feinberg, J. M., & Fox, D. L. (2016b). Max UnMix: A web application for unmixing magnetic coercivity distributions. *Computers & Geosciences*, *95*, 140–145. https://doi.org/10.1016/j.cageo.2016.07.009

Meneghini, F., Marroni, M., & Pandolfi, L. (2007). Fluid flow during accretion in sediment-dominated margins: Evidence of a high-permeability fossil fault zone from the Internal Ligurian accretionary units of the Northern Apennines, Italy. *Journal of Structural Geology*, *29*(3), 515–529. https://doi.org/10.1016/j.jsg.2006.10.003

Meneghini, F., Pandolfi, L., & Marroni, M. (2020). Recycling of heterogeneous material in the subduction factory: Evidence from the sedimentary mélange of the internal Ligurian units, Italy. *Journal of the Geological Society*, *177*(3), 587–599. https://doi.org/10.1144/jgs2019-081

Mishima, T., Hirono, T., Nakamura, N., Tanikawa, W., Soh, W., & Song, S.-R. (2009). Changes to magnetic minerals caused by frictional heating during the 1999 Taiwan Chi-Chi earthquake. *Earth Planets and Space*, *61*(6), 797–801. https://doi.org/10.1186/BF03353185

Mishima, T., Hirono, T., Soh, W., & Song, S. (2006). Thermal history estimation of the Taiwan Chelungpu fault using rock-magnetic methods. *Geophysical Research Letters*, *33*(23), 2006GL028088. https://doi.org/10.1029/2006GL028088

Mitchell, T. M., & Faulkner, D. R. (2012). Towards quantifying the matrix permeability of fault damage zones in low porosity rocks. *Earth and Planetary Science Letters*, *339–340*, 24–31. https://doi.org/10.1016/j.epsl.2012.05.014

Mittempergher, S., Cerchiari, A., Remitti, F., & Festa, A. (2018). From soft sediment deformation to fluid assisted faulting in the shallow part of a subduction megathrust analogue: The Sestola Vidiciatico tectonic unit (northern Apennines, Italy). *Geological Magazine*, *155*(2), 438–450. https://doi.org/10.1017/S0016756817000668

Moore, J. C., Rowe, C., & Meneghini, F. (2007). How accretionary prisms elucidate seismogenesis in subduction zones. In T. H. Dixon & C. Moore (Eds.), *The seismogenic zone of subduction thrust faults* (pp. 288–315). Columbia University Press. https://doi.org/10.7312/dixo13866-010

Moore, J. C., & Vrolijk, P. (1992). Fluids in accretionary prisms. *Reviews of Geophysics*, *30*(2), 113–135. https://doi.org/10.1029/92RG00201

Morin, F. J. (1950). Magnetic susceptibility of αFe_2O_3 and αFe_2O_3 with added Titanium. *Physical Review*, *78*(6), 819–820. https://doi.org/10.1103/PhysRev.78.819.2

Morris, J. D., Villinger, H. W., Klaus, A., Cardace, D. M., Chavagnac, V. M. C., Clift, P. D., et al. (2003). *Proceedings of the ocean drilling program, 205 initial reports* (Vol. 205). Ocean Drilling Program. https://doi.org/10.2973/odp.proc.ir.205.2003

Moskowitz, B. M., Frankel, R. B., & Bazylinski, D. A. (1993). Rock magnetic criteria for the detection of biogenic magnetite. *Earth and Planetary Science Letters*, *120*(3–4), 283–300. https://doi.org/10.1016/0012-821X(93)90245-5

Musgrave, R. J., Kars, M., & Vega, M. E. (2019). Progressive and punctuated magnetic mineral diagenesis: The rock magnetic record of multiple fluid inputs and progressive pyritization in a Volcano-bounded basin, IODP site U1437, Izu rear arc. *Journal of Geophysical Research: Solid Earth*, *124*(6), 5357–5378. https://doi.org/10.1029/2018JB017277

Muxworthy, A. R., & Dunlop, D. J. (2002). First-Order Reversal Curve (FORC) diagrams for pseudo-single-domain magnetites at high temperature. *Earth and Planetary Science Letters*, *203*(1), 369–382. https://doi.org/10.1016/s0012-821x(02)00880-4

Muxworthy, A. R., & McClelland, E. (2000). Review of the low-temperature magnetic properties of magnetite from a rock magnetic perspective. *Geophysical Journal International*, *140*(1), 101–114. https://doi.org/10.1046/j.1365-246x.2000.00999.x

Otake, T., Wesolowski, D. J., Anovitz, L. M., Allard, L. F., & Ohmoto, H. (2010). Mechanisms of iron oxide transformations in hydrothermal systems. *Geochimica et Cosmochimica Acta*, *74*(21), 6141–6156. https://doi.org/10.1016/j.gca.2010.07.024

Özdemir, Ö., & Dunlop, D. J. (2000). Intermediate magnetite formation during dehydration of goethite. *Earth and Planetary Science Letters*, *177*(1–2), 59–67. https://doi.org/10.1016/S0012-821X(00)00032-7

Özdemir, Ö., & Dunlop, D. J. (2014). Hysteresis and coercivity of hematite. *Journal of Geophysical Research: Solid Earth*, *119*(4), 2582–2594. https://doi.org/10.1002/2013JB010739

Özdemir, Ö., Dunlop, D. J., & Berquó, T. S. (2008). Morin transition in hematite: Size dependence and thermal hysteresis: Morin transition in hematite. *Geochemistry, Geophysics, Geosystems*, *9*(10). https://doi.org/10.1029/2008GC002110

Paterson, G. A., Zhao, X., Jackson, M., & Heslop, D. (2018). Measuring, processing, and analyzing hysteresis data. *Geochemistry, Geophysics, Geosystems*, *19*(7), 1925–1945. https://doi.org/10.1029/2018GC007620

Plesi, G. (2002). *Note illustrative Della Carta Geologica d'Italia Alla Scala 1:50.000, Foglio 235 "Pievepelago"*. Servizio Geologico d'Italia-Regione Emilia Romagna. S.EL.CA.

Plesi, G., Daniele, G., Botti, F., & Palandri, S. (2002). Carta strutturale dell'alto Appennino tosco-emiliano (scala 1:100000) fra il Passo Della Cisa e il Corno Alle Scale. In *Atti del terzo seminario sulla cartografia geologica, Bologna 2002*. SELCA.

Poulton, S. W., Krom, M. D., & Raiswell, R. (2004). A revised scheme for the reactivity of iron (oxyhydr) oxide minerals towards dissolved sulfide. *Geochimica et Cosmochimica Acta*, *68*(18), 3703–3715. https://doi.org/10.1016/j.gca.2004.03.012

Raimbourg, H., Famin, V., Palazzin, G., Mayoux, M., Jolivet, L., Ramboz, C., & Yamaguchi, A. (2018). Fluid properties and dynamics along the seismogenic plate interface. *Geosphere*, *14*(2), 469–491. https://doi.org/10.1130/GES01504.1

Ranero, C. R., Grevemeyer, I., Sahling, H., Barckhausen, U., Hensen, C., Wallmann, K., et al. (2008). Hydrogeological system of erosional convergent margins and its influence on tectonics and interplate seismogenesis. *Geochemistry, Geophysics, Geosystems*, *9*(3), 2007GC001679. https://doi.org/10.1029/2007GC001679

Remitti, F., Balestrieri, M. L., Vannucchi, P., & Bettelli, G. (2013). Early exhumation of underthrust units near the toe of an ancient erosive subduction zone: A case study from the northern Apennines of Italy. *Geological Society of America Bulletin*, *125*(11–12), 1820–1832. https://doi.org/10.1130/B30862.1

Remitti, F., Bettelli, G., Panini, F., Carlini, M., & Vannucchi, P. (2012). Deformation, fluid flow, and mass transfer in the forearc of convergent margins: A two-day field trip in an ancient and exhumed erosive convergent margin in the northern Apennines. In *Deformation, fluid flow, and mass transfer in the Forearc of convergent margins: Field guides to the Northern Apennines in Emilia and in the Apuan Alps (Italy)* (pp. 1–33). Geological Society of America. https://doi.org/10.1130/2012.0028(01

Reutter, K. J., Heinitz, I., & Ensslin, R. (1991). Structural and geothermal evolution of the Modino-Cervarola unit. *Memorie Descrittive della Carta geologica d'Italia*, *46*, 257–266.

Roberts, A. P. (2015). Magnetic mineral diagenesis. *Earth-Science Reviews*, *151*, 1–47. https://doi.org/10.1016/j.earscirev.2015.09.010

Roberts, A. P., Cui, Y., & Verosub, K. L. (1995). Wasp-waisted hysteresis loops: Mineral magnetic characteristics and discrimination of components in mixed magnetic systems. *Journal of Geophysical Research*, *100*(B9), 17909–17924. https://doi.org/10.1029/95JB00672

Roberts, A. P., Pike, C. R., & Verosub, K. L. (2000). First-order reversal curve diagrams: A new tool for characterizing the magnetic properties of natural samples. *Journal of Geophysical Research*, *105*(B12), 28461–28475. https://doi.org/10.1029/2000jb900326

Robinson, S. G. (1986). The late Pleistocene palaeoclimatic record of North Atlantic deep-sea sediments revealed by mineral-magnetic measurements. *Physics of the Earth and Planetary Interiors*, *42*(1–2), 22–47. https://doi.org/10.1016/S0031-9201(86)80006-1

Robustelli Test, C., Bilardello, D., Zanella, E., Ghignone, S., Pellegrino, L., Ferrara, E., et al. (2025). Tracing fluid-rock interactions and migration pathways in shallow megathrust shear zones through rock magnetic analysis_dataset [Dataset]. *Zenodo*. https://doi.org/10.5281/zenodo.16368514

Robustelli Test, C., & Zanella, E. (2021). Rock magnetic signature of heterogeneities across an intraplate basal contact: An example from the northern Apennines. *Geochemistry, Geophysics, Geosystems*, *22*(12), e2021GC010004. https://doi.org/10.1029/2021GC010004

Rochette, P., Fillion, G., Mattéi, J.-L., & Dekkers, M. J. (1990). Magnetic transition at 30–34 Kelvin in pyrrhotite: Insight into a widespread occurrence of this mineral in rocks. *Earth and Planetary Science Letters*, *98*(3–4), 319–328. https://doi.org/10.1016/0012-821X(90)90034-U

Saffer, D. M., & Tobin, H. J. (2011). Hydrogeology and Mechanics of subduction zone forearcs: Fluid flow and pore pressure. *Annual Review of Earth and Planetary Sciences*, *39*(1), 157–186. https://doi.org/10.1146/annurev-earth-040610-133408

Schoonen, M. A. A. (2004). Mechanisms of sedimentary pyrite formation. In J. P. Amend, K. J. Edwards, & T. W. Lyons (Eds.), *Sulfur biogeochemistry—past and present*. Geological Society of America. https://doi.org/10.1130/0-8137-2379-5.117

Screaton, E., & Saffer, D. (2005). Fluid expulsion and overpressure development during initial subduction at the Costa Rica convergent margin. *Earth and Planetary Science Letters*, *233*(3–4), 361–374. https://doi.org/10.1016/j.epsl.2005.02.017

Shi, M., Wu, H., Roberts, A. P., Zhang, S., Zhao, X., Li, H., et al. (2017). Tectonic, climatic, and diagenetic control of magnetic properties of sediments from Kumano Basin, Nankai margin, southwestern Japan. *Marine Geology*, *391*, 1–12. https://doi.org/10.1016/j.margeo.2017.07.006

Sibson, R. H. (2013). Stress switching in subduction forearcs: Implications for overpressure containment and strength cycling on megathrusts. *Tectonophysics*, *600*, 142–152. https://doi.org/10.1016/j.tecto.2013.02.035

Smirnov, A. V. (2009). Grain size dependence of low-temperature remanent magnetization in natural and synthetic magnetite: Experimental study. *Earth Planets and Space*, *61*(1), 119–124. https://doi.org/10.1186/BF03352891

Spassov, S., & Hus, J. (2006). Estimating baking temperatures in a Roman pottery kiln by rock magnetic properties: Implications of thermochemical alteration on archaeointensity determinations. *Geophysical Journal International*, *167*(2), 592–604. https://doi.org/10.1111/j.1365-246X.2006.03114.x

Tanaka, H., Hinoki, S., Kosaka, K., Lin, A., Takemura, K., Murata, A., & Miyata, T. (2001). Deformation mechanisms and fluid behavior in a shallow, brittle fault zone during coseismic and interseismic periods: Results from drill core penetrating the Nojima Fault, Japan. *Island Arc*, *10*(3–4), 381–391. https://doi.org/10.1111/j.1440-1738.2001.00336.x

Tanikawa, W., Mishima, T., Hirono, T., Soh, W., & Song, S.-R. (2008). High magnetic susceptibility produced by thermal decomposition of core samples from the Chelungpu fault in Taiwan. *Earth and Planetary Science Letters*, *272*(1–2), 372–381. https://doi.org/10.1016/j.epsl.2008.05.002

Tarling, D. H., & Hrouda, F. (1993). *The magnetic anisotropy of rocks*. Chapman & Hall.

Tartaglia, G., Viola, G., Van Der Lelij, R., Scheiber, T., Ceccato, A., & Schönenberger, J. (2020). "Brittle structural facies" analysis: A diagnostic method to unravel and date multiple slip events of long-lived faults. *Earth and Planetary Science Letters*, *545*, 116420. https://doi.org/10.1016/j.epsl.2020.116420

Thompson, R., & Oldfield, F. (1986). *Environmental magnetism*. Springer Netherlands. https://doi.org/10.1007/978-94-011-8036-8

Thomson, S. N., Brandon, M. T., Reiners, P. W., Zattin, M., Isaacson, P. J., & Balestrieri, M. L. (2010). Thermochronologic evidence for orogen-parallel variability in wedge kinematics during extending convergent orogenesis of the northern Apennines, Italy. *Geological Society of America Bulletin*, *122*(7–8), 1160–1179. https://doi.org/10.1130/B26573.1

Till, J. L., Guyodo, Y., Lagroix, F., Morin, G., & Ona-Nguema, G. (2015). Goethite as a potential source of magnetic nanoparticles in sediments. *Geology*, *43*(1), 75–78. https://doi.org/10.1130/G36186.1

Till, J. L., Moskowitz, B. M., & Jackson, M. J. (2012). High-temperature magnetic fabric development from plastically deformed magnetite in experimental shear zones: Magnetic fabric from magnetite deformation. *Geophysical Journal International*, *189*(1), 229–239. https://doi.org/10.1111/j.1365-246x.2011.05338.x

Uchida, T., Hashimoto, Y., Yamamoto, Y., & Hatakeyama, T. (2024). Exothermic events in a fossil seismogenic fault acquiring thermoviscous remanent magnetization in an exhumed accretionary complex. *Tectonophysics*, *871*, 230177. https://doi.org/10.1016/j.tecto.2023.230177

Ujiie, K., & Kimura, G. (2014). Earthquake faulting in subduction zones: Insights from fault rocks in accretionary prisms. *Progress in Earth and Planetary Science*, *1*(1), 7. https://doi.org/10.1186/2197-4284-1-7

Vannucchi, P., Remitti, F., & Bettelli, G. (2008). Geological record of fluid flow and seismogenesis along an erosive subducting plate boundary. *Nature*, *451*(7179), 699–703. https://doi.org/10.1038/nature06486

Vannucchi, P., Remitti, F., Bettelli, G., Boschi, C., & Dallai, L. (2010). Fluid history related to the early Eocene-middle Miocene convergent system of the Northern Apennines (Italy): Constraints from structural and isotopic studies. *Journal of Geophysical Research*, *115*(B5), B05405. https://doi.org/10.1029/2009JB006590

Vannucchi, P., Remitti, F., Phipps-Morgan, J., & Bettelli, G. (2009). Chapter 3 aseismic-seismic transition and fluid regime along subduction plate boundaries and a fossil example from the northern Apennines of Italy. In *International geophysics* (Vol. 94, pp. 37–68). Elsevier. https://doi.org/10.1016/S0074-6142(08)00003-X

Vannucchi, P., Sage, F., Phipps Morgan, J., Remitti, F., & Collot, J. (2012). Toward a dynamic concept of the subduction channel at erosive convergent margins with implications for interplate material transfer. *Geochemistry, Geophysics, Geosystems*, *13*(2), 2011GC003846. https://doi.org/10.1029/2011GC003846

Verwey, E. J. W. (1939). Electronic conduction of magnetite (Fe_3O_4) and its transition point at low temperatures. *Nature*, *144*(3642), 327–328. https://doi.org/10.1038/144327b0

Worm, H.-U., Clark, D., & Dekkers, M. J. (1993). Magnetic susceptibility of pyrrhotite: Grain size, field and frequency dependence. *Geophysical Journal International*, *114*(1), 127–137. https://doi.org/10.1111/j.1365-246X.1993.tb01472.x

Xu, S., & Dunlop, D. J. (1995). Toward a better understanding of the Lowrie-Fuller test. *Journal of Geophysical Research*, *100*(B11), 22533–22542. https://doi.org/10.1029/95jb02154

Xue, P., Chang, L., Pei, Z., & Harrison, R. J. (2024). The origin of magnetofossil coercivity components: Constraints from coupled experimental observations and micromagnetic calculations. *Journal of Geophysical Research: Solid Earth*, *129*(10), e2023JB028501. https://doi.org/10.1029/2023jb028501

Yamaguchi, A., Cox, S. F., Kimura, G., & Okamoto, S. (2011). Dynamic changes in fluid redox state associated with episodic fault rupture along a megasplay fault in a subduction zone. *Earth and Planetary Science Letters*, *302*(3–4), 369–377. https://doi.org/10.1016/j.epsl.2010.12.029

Yamazaki, T., & Ioka, N. (1997). Environmental rock-magnetism of pelagic clay: Implications for Asian Eolian input to the North Pacific since the Pliocene. *Paleoceanography*, *12*(1), 111–124. https://doi.org/10.1029/96pa02757

Yan, X., Zhang, B., Wang, G., Yang, T., & Chen, J. (2023). Coseismic frictional heating with concomitant hydrothermal fluid circulation revealed by rock magnetic properties of fault rocks from the rupture of the 2008 Wenchuan earthquake, China. *Geochemistry, Geophysics, Geosystems*, *24*(11), e2023GC011223. https://doi.org/10.1029/2023GC011223

Yang, T., Chen, J., Wang, H., & Jin, H. (2012a). Magnetic properties of fault rocks from the Yingxiu–Beichuan fault: Constraints on temperature rise within the shallow slip zone during the 2008 Wenchuan earthquake and their implications. *Journal of Asian Earth Sciences*, *50*, 52–60. https://doi.org/10.1016/j.jseaes.2012.01.013

Yang, T., Chen, J., Wang, H., & Jin, H. (2012b). Rock magnetic properties of fault rocks from the rupture of the 2008 Wenchuan earthquake, China and their implications: Preliminary results from the Zhaojiagou outcrop, Beichuan County (Sichuan). *Tectonophysics*, *530–531*, 331–341. https://doi.org/10.1016/j.tecto.2012.01.019

Yang, T., Chen, J., Xu, H., & Dekkers, M. J. (2019). High-velocity friction experiments indicate magnetic enhancement and softening of fault gouges during seismic slip. *Journal of Geophysical Research: Solid Earth*, *124*(1), 26–43. https://doi.org/10.1029/2018JB016341

Yang, T., Chou, Y., Ferré, E. C., Dekkers, M. J., Chen, J., Yeh, E., & Tanikawa, W. (2020). Faulting processes unveiled by magnetic properties of fault rocks. *Reviews of Geophysics*, *58*(4), e2019RG000690. https://doi.org/10.1029/2019RG000690

Yang, T., Dekkers, M. J., & Chen, J. (2018). Thermal alteration of pyrite to pyrrhotite during earthquakes: New evidence of seismic slip in the rock record. *Journal of Geophysical Research: Solid Earth*, *123*(2), 1116–1131. https://doi.org/10.1002/2017JB014973

Yang, T., Dekkers, M. J., & Zhang, B. (2016). Seismic heating signatures in the Japan trench subduction plate-boundary fault zone: Evidence from a preliminary rock magnetic geothermometer. *Geophysical Journal International*, *205*(1), 319–331. https://doi.org/10.1093/gji/ggw013

Yang, T., Yang, X., Duan, Q., Chen, J., & Dekkers, M. J. (2016). Rock magnetic expression of fluid infiltration in the Yingxiu- Beichuan fault (Longmen Shan thrust belt, China). *Geochemistry, Geophysics, Geosystems*, *17*(3), 1065–1085. https://doi.org/10.1002/2015GC006095

Zamani, N., Heij, G. W., Ferré, E. C., Murphy, M. A., & Bagley, B. (2023). High-velocity slip and thermal decomposition of carbonates: Example from the Heart Mountain Slide ultracataclasites, Wyoming. *Journal of Geophysical Research: Solid Earth*, *128*(5), e2022JB026185. https://doi.org/10.1029/2022JB026185

Zhang, L., Sun, Z., Li, H., Zhao, L., Song, S., Chou, Y., et al. (2017). Rock record and magnetic response to large earthquakes within Wenchuan earthquake fault scientific drilling cores. *Geochemistry, Geophysics, Geosystems*, *18*(5), 1889–1906. https://doi.org/10.1002/2017GC006822

Zhao, X., Oda, H., Wu, H., Yamamoto, T., Yamamoto, Y., Yamamoto, Y., et al. (2013). Magnetostratigraphic results from sedimentary rocks of IODP's Nankai Trough Seismogenic Zone Experiment (NanTroSEIZE) expedition 322. *Geological Society, London, Special Publications*, *373*(1), 191–243. https://doi.org/10.1144/SP373.14

References From the Supporting Information

Banerjee, S. K., King, J., & Marvin, J. (1981). A rapid method for magnetic granulometry with applications to environmental studies. *Geophysical Research Letters*, *8*(4), 333–336. https://doi.org/10.1029/GL008i004p00333

Carter-Stiglitz, B., Jackson, M., & Moskowitz, B. (2002). Low-temperature remanence in stable single domain magnetite. *Geophysical Research Letters*, *29*(7). https://doi.org/10.1029/2001GL014197

Carter-Stiglitz, B., Moskowitz, B., Solheid, P., Berquó, T. S., Jackson, M., & Kosterov, A. (2006). Low-temperature magnetic behavior of multidomain titanomagnetites: TM0, TM16, and TM35. *Journal of Geophysical Research*, *111*(B12), 2006JB004561. https://doi.org/10.1029/2006JB004561

Channell, J. E. T. (2007). Paleomagnetism, deep-sea sediments. In D. Gubbins & E. Herrero-Bervera (Eds.), *Encyclopedia of geomagnetism and paleomagnetism* (pp. 781–788). Springer Netherlands. https://doi.org/10.1007/978-1-4020-4423-6_186

Clark, D. A. (1984). Hysteresis properties of sized dispersed monoclinic pyrrhotite grains. *Geophysical Research Letters*, *11*(3), 173–176. https://doi.org/10.1029/GL011i003p00173

Dankers, P. (1981). Relationship between median destructive field and remanent coercive forces for dispersed natural magnetite, titanomagnetite and hematite. *Geophysical Journal International*, *64*(2), 447–461. https://doi.org/10.1111/j.1365-246X.1981.tb02676.x

Dearing, J. A. (1999). Magnetic susceptibility. In J. Walden, F. Oldfield, & J. P. Smith (Eds.), *Environmental magnetism: A practical guide* (pp. 35–62). Quat. Res. Ass.

Dekkers, M. J., & Schoonen, M. A. A. (1996). Magnetic properties of hydrothermally synthesized greigite (Fe_3S_4) I. Rock magnetic parameters at room temperature. *Geophysical Journal International*, *126*(2), 360–368. https://doi.org/10.1111/j.1365-246X.1996.tb05296.x

Dekkers, M. J. (1988). Magnetic properties of natural pyrrhotite Part I: Behavior of initial susceptibility and saturation-magnetization-related rock-magnetic parameters in a grain size dependent framework. *Physics of the Earth and Planetary Interiors*, *52*(3–4), 376–393. https://doi.org/10.1016/0031-9201(88)90129-X

Dekkers, M. J. (1989a). Magnetic properties of natural goethite-I. Grain size dependence of some low- and high-field related rockmagnetic parameters measured at room temperature. *Geophysical Journal International*, *97*(2), 323–340. https://doi.org/10.1111/j.1365-246X.1989.tb00504.x

Dunlop, D. J., & Özdemir, Ö. (1997). *Rock magnetism: Fundamentals and frontiers*. Cambridge University Press.

Dunlop, D. J., & Özdemir, Ö. (2018). Remanence cycling of 0.6–135 μm magnetites across the Verwey transition. *Earth Planets and Space*, *70*(1), 164. https://doi.org/10.1186/s40623-018-0928-z

Dunlop, D. J., Özdemir, Ö., & Xu, S. (2019). Magnetic hysteresis of 0.6–110 μm magnetites across the Verwey transition. *Canadian Journal of Earth Sciences*, *56*(9), 958–972. https://doi.org/10.1139/cjes-2018-0088

Dunlop, D. J. (1986). Hysteresis properties of magnetite and their dependence on particle size: A test of pseudo-single-domain remanence models. *Journal of Geophysical Research*, *91*(B9), 9569–9584. https://doi.org/10.1029/JB091iB09p09569

Dunlop, D. J. (2021). Magnetic hysteresis of magnetite, pyrrhotite and hematite at high temperature. *Geophysical Journal International*, *225*(1), 1–14. https://doi.org/10.1093/gji/ggaa569

Egli, R. (2003). Analysis of the field dependence of remanent magnetization curves. *Journal of Geophysical Research*, *108*(B2), 2002JB002023. https://doi.org/10.1029/2002JB002023

Egli, R. (2004b). Characterization of individual rock magnetic components by analysis of remanence curves. 3. Bacterial magnetite and natural processes in lakes. *Physics and Chemistry of the Earth, Parts A/B/C*, *29*(13–14), 869–884. https://doi.org/10.1016/j.pce.2004.03.010

Evans, M. E., & Heller, F. (2003). *Environmental magnetism: Principles and applications of enviromagnetics*. Academic Press.

Guyodo, Y., Gaillot, P., & Channell, J. E. T. (2000). Wavelet analysis of relative geomagnetic paleointensity at ODP Site 983. *Earth and Planetary Science Letters*, *184*(1), 109–123. https://doi.org/10.1016/S0012-821X(00)00313-7

Halgedahl, S. L., & Jarrard, R. D. (1995). Low-temperature behavior of single-domain through multidomain magnetite. *Earth and Planetary Science Letters*, *130*(1–4), 127–139. https://doi.org/10.1016/0012-821X(94)00260-6

Hartstra, R. L. (1983). TRM, ARM and Isr of two natural magnetites of MD and PSD grain size. *Geophysical Journal International*, *73*(3), 719–737. https://doi.org/10.1111/j.1365-246X.1983.tb03342.x

Heider, F., Dunlop, D. J., & Soffel, H. C. (1992). Low-temperature and alternating field demagnetization of saturation remanence and thermoremanence in magnetite grains (0.037 μm to 5 mm). *Journal of Geophysical Research*, *97*(B6), 9371–9381. https://doi.org/10.1029/91JB03097

Heller, F. (1978). Rockmagnetic studies of Upper Jurassic limestones from southern Germany. *Journal of Geophysics*, *44*(1), 525–543.

Hrouda, F., Chlupáčová, M., & Novák, J. K. (2002). Variations in magnetic anisotropy and opaque mineralogy along a kilometer deep profile within a vertical dyke of the syenogranite porphyry at Cínovec (Czech Republic). *Journal of Volcanology and Geothermal Research*, *113*(1–2), 37–47. https://doi.org/10.1016/S0377-0273(01)00249-9

Hrouda, F. (2002). Low-field variation of magnetic susceptibility and its effect on the anisotropy of magnetic susceptibility of rocks. *Geophysical Journal International*, *150*(3), 715–723. https://doi.org/10.1046/j.1365-246X.2002.01731.x

Hrouda, F. (2003). Indices for numerical characterization of the alteration processes of magnetic minerals taking place during investigation of temperature variation of magnetic susceptibility. *Studia Geophysica et Geodaetica*, *47*(4), 847–861. https://doi.org/10.1023/A:1026398920172

Hunt, C. P., Moskowitz, B. M., & Banerjee, S. K. (1995). Magnetic properties of rocks and minerals. In T. J. Ahrens (Ed.), *AGU reference shelf* (pp. 189–204). American Geophysical Union. https://doi.org/10.1029/RF003p0189

Kars, M., & Kodama, K. (2015a). Authigenesis of magnetic minerals in gas hydrate-bearing sediments in the Nankai Trough, offshore Japan. *Geochemistry, Geophysics, Geosystems*, *16*(3), 947–961. https://doi.org/10.1002/2014GC005614

Kars, M., & Kodama, K. (2015b). Rock magnetic characterization of ferrimagnetic iron sulfides in gas hydrate-bearing marine sediments at Site C0008, Nankai Trough, Pacific Ocean, off-coast Japan. *Earth Planets and Space*, *67*(1), 118. https://doi.org/10.1186/s40623-015-0287-y

Kars, M., Aubourg, C., & Pozzi, J.-P. (2011). Low temperature magnetic behavior near 35 K in unmetamorphosed claystones: <50 K magnetic behavior. *Geophysical Journal International*, *186*(3), 1029–1035. https://doi.org/10.1111/j.1365-246X.2011.05121.x

Kars, M., Aubourg, C., Pozzi, J., & Janots, D. (2012). Continuous production of nanosized magnetite through low grade burial. *Geochemistry, Geophysics, Geosystems*, *13*(8), 2012GC004104. https://doi.org/10.1029/2012GC004104

Kars, M., Musgrave, R. J., Hoshino, T., Jonas, A., Bauersachs, T., Inagaki, F., & Kodama, K. (2018). Magnetic mineral diagenesis in a high temperature and deep methanic zone in Izu rear arc marine sediments, Northwest Pacific ocean. *Journal of Geophysical Research: Solid Earth*, *123*(10), 8331–8348. https://doi.org/10.1029/2018JB015861

King, J., Banerjee, S. K., Marvin, J., & Özdemir, Ö. (1982). A comparison of different magnetic methods for determining the relative grain size of magnetite in natural materials: Some results from lake sediments. *Earth and Planetary Science Letters*, *59*(2), 404–419. https://doi.org/10.1016/0012-821x(82)90142-x

King, J. W., Banerjee, S. K., & Marvin, J. (1983). A new rock-magnetic approach to selecting sediments for geomagnetic paleointensity studies: Application to paleointensity for the last 4000 years. *Journal of Geophysical Research*, *88*(B7), 5911–5921. https://doi.org/10.1029/JB088iB07p05911

Kruiver, P. P., & Passier, H. F. (2001). Coercivity analysis of magnetic phases in sapropel S1 related to variations in redox conditions, including an investigation of the *S* ratio. *Geochemistry, Geophysics, Geosystems*, *2*(12), 2001GC000181. https://doi.org/10.1029/2001GC000181

Larrasoaña, J. C., Roberts, A. P., Musgrave, R. J., Gràcia, E., Piñero, E., Vega, M., & Martínez-Ruiz, F. (2007). Diagenetic formation of greigite and pyrrhotite in gas hydrate marine sedimentary systems. *Earth and Planetary Science Letters*, *261*(3–4), 350–366. https://doi.org/10.1016/j.epsl.2007.06.032

Lascu, I., Banerjee, S. K., & Berquó, T. S. (2010). Quantifying the concentration of ferrimagnetic particles in sediments using rock magnetic methods. *Geochemistry, Geophysics, Geosystems*, *11*(8), 2010GC003182. https://doi.org/10.1029/2010GC003182

Liu, Q., Roberts, A. P., Larrasoaña, J. C., Banerjee, S. K., Guyodo, Y., Tauxe, L., & Oldfield, F. (2012). Environmental magnetism: Principles and applications. *Reviews of Geophysics*, *50*(4), 2012RG000393. https://doi.org/10.1029/2012RG000393

Lu, R., & Banerjee, S. K. (1994). Magnetite dissolution in deep sediments and its hydrologic implication: A detailed study of sediments from site 808, leg 131. *Journal of Geophysical Research*, *99*(B5), 9051–9059. https://doi.org/10.1029/93JB03204

Maher, B. A. & Thompson, R. (Eds.) (1999)., *Quaternary climates, environments, and magnetism*. Cambridge University Press.

Maher, B. A., Karloukovski, V. V., & Mutch, T. J. (2004). High-field remanence properties of synthetic and natural submicrometre haematites and goethites: Significance for environmental contexts. *Earth and Planetary Science Letters*, *226*(3–4), 491–505. https://doi.org/10.1016/j.epsl.2004.05.042

Maher, B. A. (2007). Environmental magnetism and climate change. *Contemporary Physics*, *48*(5), 247–274. https://doi.org/10.1080/00107510801889726

Moskowitz, B. M. (2007). Magnetization, anhysteretic remanent. In D. Gubbins & E. Herrero-Bervera (Eds.), *Encyclopedia of geomagnetism and paleomagnetism* (pp. 572–580). Springer Netherlands. https://doi.org/10.1007/978-1-4020-4423-6_186

Muxworthy, A. R., Dunlop, D. J., & Özdemir, Ö. (2003). Low-temperature cycling of isothermal and anhysteretic remanence: Microcoercivity and magnetic memory. *Earth and Planetary Science Letters*, *205*(3–4), 173–184. https://doi.org/10.1016/S0012-821X(02)01039-7

Oldfield, F. (1994). Toward the discrimination of fine-grained ferrimagnets by magnetic measurements in lake and near-shore marine sediments. *Journal of Geophysical Research*, *99*(B5), 9045–9050. https://doi.org/10.1029/93jb03137

Özdemir, Ö., & Dunlop, D. J. (2010). Hallmarks of maghemitization in low-temperature remanence cycling of partially oxidized magnetite nanoparticles. *Journal of Geophysical Research*, *115*(B2), 2009JB006756. https://doi.org/10.1029/2009JB006756

Peters, C., & Dekkers, M. J. (2003). Selected room temperature magnetic parameters as a function of mineralogy, concentration and grain size. *Physics and Chemistry of the Earth, Parts A/B/C*, *28*(16–19), 659–667. https://doi.org/10.1016/S1474-7065(03)00120-7

Pokorný, J., Pokorný, P., Suza, P., & Hrouda, F. (2011). A Multi-function Kappabridge for high precision measurement of the AMS and the variations of magnetic susceptibility with field, temperature and frequency. In E. Petrovský, D. Ivers, T. Harinarayana, & E. Herrero-Bervera (Eds.), *The earth's magnetic interior* (pp. 293–301). Springer Netherlands. https://doi.org/10.1007/978-94-007-0323-0_20

Roberts, A. P., Stoner, J. S., & Richter, C. (1999). Diagenetic magnetic enhancement of sapropels from the eastern Mediterranean Sea. *Marine Geology*, *153*(1–4), 103–116. https://doi.org/10.1016/S0025-3227(98)00087-5

Roberts, A. P., Liu, Q., Rowan, C. J., Chang, L., Carvallo, C., Torrent, J., & Horng, C. (2006). Characterization of hematite (α -Fe_2O_3), goethite (α -FeOOH), greigite (Fe_3S_4), and pyrrhotite (Fe_7S_8) using first-order reversal curve diagrams. *Journal of Geophysical Research*, *111*(B12), 2006JB004715. https://doi.org/10.1029/2006JB004715

Roberts, A. P., Chang, L., Rowan, C. J., Horng, C., & Florindo, F. (2011). Magnetic properties of sedimentary greigite (Fe_3S_4): An update. *Reviews of Geophysics*, *49*(1), 2010RG000336. https://doi.org/10.1029/2010RG000336

Roberts, A. P., Hu, P., Harrison, R. J., Heslop, D., Muxworthy, A. R., Oda, H., et al. (2019). Domain state diagnosis in rock magnetism: Evaluation of potential alternatives to the day diagram. *Journal of Geophysical Research: Solid Earth*, *124*(6), 5286–5314. https://doi.org/10.1029/2018JB017049

Roberts, A. P. (1995). Magnetic properties of sedimentary greigite (Fe_3S_4). *Earth and Planetary Science Letters*, *134*(3–4), 227–236. https://doi.org/10.1016/0012-821X(95)00131-U

Robertson, D. J., & France, D. E. (1994). Discrimination of remanence-carrying minerals in mixtures, using isothermal remanent magnetisation acquisition curves. *Physics of the Earth and Planetary Interiors*, *82*(3–4), 223–234. https://doi.org/10.1016/0031-9201(94)90074-4

Sagnotti, L. (2007). Iron sulfides. In D. Gubbins & E. Herrero-Bervera (Eds.), *Encyclopedia of geomagnetism and paleomagnetism* (pp. 454–460). Springer Netherlands. https://doi.org/10.1007/978-1-4020-4423-6_186

Snowball, I. F. (1991). Magnetic hysteresis properties of greigite (Fe_3S_4) and a new occurrence in Holocene sediments from Swedish Lappland. *Physics of the Earth and Planetary Interiors*, *68*(1–2), 32–40. https://doi.org/10.1016/0031-9201(91)90004-2

Stober, J. C., & Thompson, R. (1979). An investigation into the source of magnetic minerals in some Finnish lake sediments. *Earth and Planetary Science Letters*, *45*(2), 464–474. https://doi.org/10.1016/0012-821X(79)90145-6

Sugiura, N. (1979). ARM, TRM and magnetic interactions: Concentration dependence. *Earth and Planetary Science Letters*, *42*(3), 451–455. https://doi.org/10.1016/0012-821X(79)90054-2

Tauxe, L., Bertram, H. N., & Seberino, C. (2002). Physical interpretation of hysteresis loops: Micromagnetic modeling of fine particle magnetite. *Geochemistry, Geophysics, Geosystems*, *3*(10), 1055. https://doi.org/10.1029/2001GC000241

Thompson, R., Stober, J. C., Turner, G. M., Oldfield, F., Bloemendal, J., Dearing, J. A., & Rummery, T. A. (1980). Environmental applications of magnetic measurements. *Science*, *207*(4430), 481–486. https://doi.org/10.1126/science.207.4430.481

Verosub, K. L., & Roberts, A. P. (1995). Environmental magnetism: Past, present, and future. *Journal of Geophysical Research*, *100*(B2), 2175–2192. https://doi.org/10.1029/94JB02713

Wang, D., & Van der Voo, R. (2004). The hysteresis properties of multidomain magnetite and titanomagnetite/titanomaghemite in mid-ocean ridge basalts. *Earth and Planetary Science Letters*, *220*(1–2), 175–184. https://doi.org/10.1016/S0012-821X(04)00052-4